Pathway and mechanism of tubulin folding mediated by TRiC/CCT conjugated with its ATPase cycle revealed by cryo-EM

Caixuan Liu[1,2], Mingliang Jin[1], Shutian Wang[1,2], Wenyu Han[1,2], Qiaoyu Zhao[1,2], Yifan Wang[1,2], Cong Xu[1,2], Lei Diao[3], Yue Yin[4], Chao Peng[4], Lan Bao[2,3], Yanxing Wang[1], Yao Cong[1,2]*

[1] State Key Laboratory of Molecular Biology, National Center for Protein Science Shanghai, Shanghai Institute of Biochemistry and Cell Biology, Center for Excellence in Molecular Cell Science, Chinese Academy of Sciences, Shanghai 200031, China.

[2] University of Chinese Academy of Sciences, Beijing 100049, China.

[3] State Key Laboratory of Cell Biology, Shanghai Institute of Biochemistry and Cell Biology, Center for Excellence in Molecular Cell Science, Chinese Academy of Sciences, Shanghai 200031, China.

[4] National Facility for Protein Science in Shanghai, Zhangjiang Lab, Shanghai Advanced Research Institute, CAS, Shanghai 201210, China.

*Address correspondence to Yao Cong, cong@sibcb.ac.cn

Abstract

The eukaryotic chaperonin TRiC/CCT assists the folding of about 10% of cytosolic proteins through an ATP-driven conformational cycle, and the essential cytoskeleton protein tubulin is the obligate substrate of TRiC. Here, we present an ensemble of cryo-EM structures of human TRiC throughout its ATPase cycle, with three of them revealing endogenously engaged tubulin in different folding stages. Our structural and XL-MS analyses suggested a gradual upward translocation and stabilization of tubulin within the TRiC chamber accompanying TRiC ring closure. Remarkably, in the closed TRiC-tubulin-S3 map resolved to 3.1-Å-resolution, we captured a near-natively folded tubulin. We found the near-natively folded tubulin engaging through its N and C domains mainly with the A and I domains of the CCT3/6/8 subunits through electrostatic and hydrophilic interactions, while the tubulin I domain was found to remain dynamic. Moreover, we also showed the potential role of TRiC C-terminal tails in substrate stabilization and folding. Our study delineates the pathway and molecular mechanism of TRiC-mediated tubulin folding conjugated with TRiC ATPase cycle, and may also inform the design of therapeutic agents targeting TRiC-tubulin interactions.

Introduction

Chaperonins are protein folding nanomachines that play an essential role in maintaining cellular homeostasis and are important in all kingdoms of life, and their dysfunction is closely related to cancer and neurodegenerative diseases[1-3]. Chaperonins provide a cage-like environment for proteins to fold in isolation, unimpaired by aggregation, and in some cases actively modulate the folding pathway of the encapsulated protein[4-7]. The eukaryotic group II chaperonin TRiC/CCT assists the folding of ~10% of cytosolic proteins, including the key cytoskeletal proteins actin and tubulin, cell cycle regulator CDC20, and VHL tumor suppressor[8-15]. TRiC is the most complex chaperon system identified to date. It has a double-ring structure, and each ring consists of eight paralogous subunits (namely CCT1-CCT8) arranged in a specific order[16-21]. Each TRiC subunit consists of three domains: the substrate-recognition apical domain (A domain) and the ATP-binding equatorial domain (E domain) linked by the intermediate domain (I domain). TRiC-mediated substrate folding is closely related to its ATP-driven conformational cycle[22-25]. TRiC has been proved to display subunit specificity in the complex assembly, ATP consumption and ring closure[16,19,26,27].

In the past two decades, constant efforts have been made to capture the TRiC-substrate binary complexes so as to reveal the mechanism of TRiC-assisted substrate folding for diverse substrates[7,9,11,15,28-32]. Still, there remains lacking of the atomic-resolution structural details revealing the dynamic process of TRiC-mediated substrate folding throughout its ATP-driven conformational cycle, due to the relative low binding efficiency between TRiC and the pretreated unfolded substrates (usually involving applying urea or GuHCl *in vitro*) and due to the potential conformational and compositional heterogeneity of the binary complex[33].

Tubulin, the building block of microtubule, is the *in vivo* obligate substrate of TRiC[15,34-37]. Highly conserved α- and β-tubulin heterodimers assemble into dynamic microtubules[38] , which are ubiquitous cytoskeletal polymers essential for the life of all eukaryotic cells. Microtubules are involved in a wide range of cellular functions, from cell motility and intracellular transport to, most fundamentally, cell division[36,39-43].

Tubulin (~50 kDa) contains three domains: the GTP-binding N domain, the I domain containing the site that binds the chemotherapeutic Taxol, and the C domain responsible for interacting with microtubule-binding proteins. Previous studies reported structures of the TRiC-tubulin complex in the apo or ATP-binding state at relatively low resolution (~25 Å) or intermediate resolution (5.5 Å) determined using cryo-electron microscopy (cryo-EM) or X-ray crystallography[9,15,32]. However, a complete picture with molecular details of the TRiC-directed tubulin folding driven by ATP binding and hydrolysis remains obscure. Moreover, it has been reported that the small molecule I-Trp can disrupt constitutively associated β-tubulin/TRiC, causing severe cell apoptosis, indicating that targeting the TRiC/tubulin complex could serve as a novel chemotherapeutic strategy[44,45].

To capture the TRiC-directed tubulin folding pathway, we determined an ensemble of cryo-EM structures of human TRiC (hTRiC) throughout its ATP-driven conformational cycle. Three of these structures showed endogenously bound tubulin. Strikingly, in the closed-state TRiC-tubulin-S3 structure, we captured a near-natively folded tubulin and disclosed atomic details of the interaction between tubulin and TRiC. We also found that the C- and N-terminal tails (abbreviated as C-/N-termini) of TRiC play distinct roles in substrate stabilization/folding and TRiC allosteric coordination, respectively, with the N-terminus of CCT8 possibly contributing to tubulin folding in the opposite ring. Collectively, our study captured a thorough picture of the pathway and molecular mechanism of TRiC-mediated tubulin folding conjugated with the TRiC ATPase cycle.

Results

Cryo-EM structure of TRiC in complex with tubulin

We purified endogenous human TRiC from HEK293F cells (Extended Data Fig. 1a; hereafter, "TRiC" refers to human TRiC unless otherwise noted), which was validated by sodium dodecyl sulfate-polyacrylamide gel electrophoresis (SDS-PAGE) and mass spectrometry (MS) analyses (Fig. 1a and Supplementary Table 1). The result

92 of NADH-coupled enzymatic assay further validated the ATPase activity of the purified
93 TRiC (Extended Data Fig. 1b). Moreover, our SDS-PAGE analysis also indicated the
94 presence of an extra associated protein at ~50 kDa (Fig. 1a), which was suggested to be
95 mainly β-tubulin (TUBB5) by the MS analysis (Supplementary Table 1). The PSM
96 value from the MS analysis, indicating the relative abundance of a certain protein[46],
97 showed the abundance of β-tubulin was comparable to that of individual TRiC subunit.
98 The existence of tubulin was further confirmed by native electrophoresis combined with
99 western blot and chemical cross-linking-coupled mass spectrometry (XL-MS) analysis
100 (Fig. 1b-c, Supplementary Table 2). Our XL-MS analysis detected five cross-links
101 between tubulin and CCT3/4/6/8 subunits (Fig. 1c). Taken together, these data indicated
102 a co-existence of TRiC with tubulin.

103 We then performed cryo-EM study on the endogenously purified TRiC sample
104 (Extended Data Fig. 1c). Two cryo-EM maps, including an open state TRiC with an
105 empty chamber, and another TRiC map also in the open conformation but displaying
106 an extra density in one chamber, were determined at 3.1- and 4.1-Å-resolution,
107 respectively (Fig. 1d-g, and Extended Data Fig. 2). Interestingly, although we
108 performed buffer exchange multiple times to remove remaining nucleotide in the final
109 stage of purification, CCT3/6/8 subunits appeared to have bound nucleotide density in
110 both maps (Extended Data Fig. 3e-f), which were suggested to be ADP according to an
111 ADP/ATP ratio assay (Extended Data Fig. 3g), in line with our previous report on the
112 yeast TRiC system[19]. Accordingly, these two open TRiC maps are also in the
113 "nucleotide partially preloaded" (NPP) state. We then denoted the free open TRiC map
114 as TRiC-NPP. The NPP state is equivalent to the "apo" state in typical conformational
115 cycle studies of ATPase chaperonins[24,47,48], mimicking the starting point in the
116 conformational cycle of the chaperonin itself.

117 Our TRiC-NPP map showed a conformation overall similar to that of the available
118 substrate-free human TRiC cryo-EM map also in the open state at 7.7-Å-resolution,
119 with determined subunit assignment[49]. We then fit the TRiC-NPP map to their map
120 (Extended Data Fig. 4a), both displaying the following characteristic features known

121 for open-state TRiC: (1) CCT1 being the most outward tilted subunit, a feature common
122 for yeast, bovine, and human TRiCs[16,19,7,49]; (2) the A domain of CCT2 being quite
123 disordered (Fig. 1d), also observed in open bovine TRiC[7,24]; (3) each ring displaying a
124 tetramer-of-dimer pattern as in the open bovine TRiC[24]; (4) the largest gap existing
125 between CCT1 and CCT4[50] (Extended Data Fig. 4b). These features allowed us to
126 assign the subunits for the TRiC-NPP map. We then built an atomic model for TRiC-
127 NPP (Extended Data Fig. 3a-d). Further inspection of the TRiC-NPP structure revealed
128 the characteristic V476-K484 insertion in the E domain of CCT1 (Extended Data Fig.
129 4c-d), corroborating our subunit assignment for this map.

130 Moreover, our TRiC-NPP map showed a chunk of density between the two
131 equators blocking the two chambers (Fig. 1e), with this density symmetrically
132 contacting the N-/C-terminal extensions of CCT5/7 and CCT5'/7' from both rings of
133 TRiC (Extended Data Fig. 4e). Hence, we assigned the density as the unstructured N-
134 and C-terminal tails of TRiC subunits, also observed in the available human and bovine
135 TRiC open-state maps[7,49] (Extended Data Fig. 4f-g). Moreover, the A/I domains of
136 CCT2 hemisphere subunits (including CCT4/2/5/7)[21,28] appeared less well resolved as
137 in the bovine and human open-state TRiC structures[7,24,28,49], indicating an intrinsic
138 dynamic nature in these regions. Indeed, our 3D variability analysis (3DVA) using
139 cryoSPARC[51] suggested the A/I domains of CCT1/4/2/5/7 to be overall relatively
140 dynamic—and strikingly, with those of CCT7/5/1 showing continuous outward/inward
141 tilting motions of up to ~23°/6°/5°, respectively (Extended Data Fig. 4h and
142 Supplementary Video 1).

143 Importantly, for the other map derived from the same dataset (38.4% of the
144 population, Fig. 1f-g and Extended Data Fig. 2a), we attributed the captured extra
145 density in the cis-ring chamber to the trapped β-tubulin co-purified with TRiC, based
146 on our biochemical and MS data (Fig. 1a-c, Extended Data Fig. 4i and Supplementary
147 Table 1-2). We denoted this map as TRiC-tubulin-S1, which was also in the NPP state
148 with the consecutive CCT3/6/8 subunits loaded with nucleotides in both rings
149 (Extended Data Fig. 3f). This demonstrated that TRiC can engage with substrate in the

150 nucleotide partially loaded NPP state. A previous crystal structure of bovine TRiC with
151 bound tubulin also revealed two nucleotides per-ring in non-consecutive subunits[15]. The
152 TRiC conformation in the S1 map was observed to resemble that of our TRiC-NPP
153 structure (Extended Data Fig. 4j), we then followed the same subunit assignment.
154 Overall, the substrate density appeared to associate with the E domain of every TRiC
155 subunit, mainly with the C-terminus and stem loop of these subunits (Fig. 1h). The
156 bovine TRiC-tubulin crystal structure also revealed that the tubulin forms contact with
157 the stem loops of three TRiC subunits[15].

158 **Tubulin translocation within TRiC chamber accompanying TRiC conformational**
159 **cycle**

160 To further capture the TRiC-directed tubulin folding process conjugated with TRiC
161 ATPase cycle, we performed cryo-EM study on TRiC in the presence of 1 mM ATP-
162 AlFx (Extended Data Fig. 1d), an ATP-hydrolysis-transition state analog that can
163 trigger TRiC ring closure[22,23,25]. In the resulting dataset, the majority (65.4%) of the
164 particles were in the closed conformation and resolved to a resolution of 2.9 Å, while
165 the remaining (34.6%) particles were in the open conformation and resolved to a
166 resolution of 4.2 Å (Fig. 2a and Extended Data Fig. 5a-c). In the open state, obvious
167 substrate density was observed in the cis-ring, and we denoted this map as TRiC-
168 tubulin-S2. For the closed state, through focused classification in the chamber region,
169 we obtained two maps: one map at a resolution of 3.1 Å showed tubulin density in the
170 cis-ring chamber (termed TRiC-tubulin-S3), and the other map at a resolution of 3.2 Å
171 showed no substrate in the chamber, but a central tail density in an orientation different
172 from that in the open state (denoted as TRiC-ADP-AlFx, discussed below) (Fig. 2c-g,
173 Extended Data Fig. 5a-b, d-f). Moreover, we performed XL-MS analysis on the ATP-
174 AlFx presented TRiC sample, and detected 17 cross-links between tubulin and TRiC
175 subunits (Fig. 2h and Supplementary Table 3), further substantiating the notion that the
176 captured substrate was indeed tubulin.

177 The overall TRiC conformation of the open-state S2 map was observed to be
178 similar to that of the TRiC-NPP map (Extended Data Fig. 5g). We then followed the

179 subunit assignments of TRiC-NPP to assign those of S2. For the closed-state S3 map, a
180 characteristic kink feature in the CCT6 α-helical protrusion H8 and the unique
181 insertions in CCT1/4/6 were clearly visualized (Extended Data Fig. 6), facilitating the
182 subunit assignment in the maps of the closed TRiC with similar features. We then built
183 an atomic model for each of the S2, S3 and TRiC-ADP-AlFx maps (Extended Data Fig.
184 7a-f). We found that for these three structures, all subunits from both rings bound
185 nucleotides (Extended Data Fig. 7g-i). For the S2 map, the nucleotide density was fitted
186 well by the ATP structure (Extended Data Fig. 7j), indicating S2 was in the ATP-binding
187 state. For the closed S3 and TRiC-ADP-AlFx structures, with their E-domain local
188 resolution reached ~2.8 to 2.9 Å (Extended Data Fig.5d-e), the nucleotide densities for
189 all subunits matched ADP-AlFx and a magnesium ion very well, in addition to a water
190 molecule attacking the γ-phosphate of nucleotide, involved in the formation of the ATP
191 hydrolysis reaction center (Fig. 2i and Extended Data Fig. 7k). These features suggested
192 the two closed-state maps were in the ATP hydrolysis transition state.

193 Indeed, the CCT2 subunit in the S2 map appeared less dynamic and better resolved
194 than that in the NPP-state S1 map (Figs. 1d, f and Fig. 2a), indicating CCT2 may have
195 been stabilized after ATP binding. Accordingly, the substrate density in the S2 map
196 appeared larger than that in the S1 map, with this difference attributed to ATP-binding-
197 induced stabilization of TRiC (Fig. 1h and Fig. 2j). Notably, in TRiC-tubulin-S2, the
198 substrate density was found to be closely associated with all the three domains of
199 CCT6/8 and to form loose contacts with the E domains of the other subunits (Fig. 2j)
200 as well as with the central tail region (Fig. 2b). Compared with TRiC-tubulin-S1, it
201 appears that ATP-binding could drive tubulin to translocate from the E domains of all
202 the subunits slightly up towards the A/I domains, to converge more on the CCT6/8
203 subunits, while nevertheless remaining bound to all of the E domains (Fig. 2j).

204 **ATP-driven TRiC ring closure is the determinant step for tubulin folding**

205 Importantly, inspection of our TRiC-tubulin-S3 map revealed a well resolved
206 tubulin density in one chamber of TRiC hanging underneath its dome predominantly
207 on the CCT6 hemisphere subunits (including CCT1/3/6/8)[21,28] (Fig. 2d-e and Fig. 3a-

208 b). The tubulin density appeared to resemble the conformation of native tubulin (Fig.
209 3b), and hence we defined the captured tubulin as being in the near-natively folded state.
210 Overall, the N and C domains of tubulin were relatively well resolved with atomic
211 details observed (Fig. 3c). While the majority of the I domain of tubulin was captured
212 (Fig. 3b), a small portion (sequence: 242-249, 279-283, 319-348) facing the central
213 chamber was less well resolved (Fig. 3a, d), implying an intrinsically dynamic nature
214 for this region. Interestingly, this dynamic region was noted to overlap with its
215 interaction interface with α-tubulin to form a tubulin heterodimer or with cofactor A for
216 the release of tubulin[43,52] (Fig. 3d), indicating this intrinsically dynamic region of the
217 tubulin I domain may only be stabilized by engaging with these factors. Substantiating
218 this speculation, our XL-MS analysis showed that tubulin I domain Lys252 forms
219 crosslinks with all subunits of TRiC with the cross-linked Cα-Cα distances ranging
220 from 20 to 61 Å (Fig. 3e), indicating a highly dynamic structure in this region. These
221 results were also in line with a recent report showing reovirus σ3 capsid protein acting
222 as a dynamic substrate within the TRiC chamber[28]. Note that this Lys252 had been
223 shown to play an essential role in interacting with the γ-phosphate of the GTP in the α-
224 tubulin portion of the tubulin dimer[43] (Fig. 3f). Collectively, our data suggested that the
225 I domain region of β-tubulin is intrinsically dynamic since it is "born" before
226 associating with α-tubulin to form the tubulin dimer.

227 Inspection of the S3 map showed that tubulin engages with TRiC mainly through
228 its N/C domains, forming intimate salt-bridge- and H-bond-mediated contacts with all
229 three domains of the CCT6 hemisphere subunits (Fig. 3g, h and Supplementary Table
230 4). The tubulin I domain also loosely interacts with CCT2 hemisphere subunits through
231 association with the A-domain protrusion loop and C-termini of CCT7/5/2/4 (Fig. 3g).
232 Indeed, tubulin showed an obviously larger interaction area with the CCT6 hemisphere
233 subunits than with the CCT2 hemisphere ones (Extended Data Fig. 7l). Furthermore,
234 inspection of S3 structure also unprecedently revealed the protrusion loop, $loop^{H10}$,
235 $loop^{H9}$, C-terminus, and stem loop to be the main structural elements of TRiC involved
236 in its interaction with tubulin (Fig. 3g-h and Extended Data Fig. 7m-n). Our TRiC-

237 tubulin-S3 structure appeared overall comparable with a recent structure of closed
238 TRiC-tubulin complex[53], in terms of tubulin orientation and binding location within
239 TRiC chamber.

240 In addition, our XL-MS data suggested that before adding nucleotide, tubulin only
241 crossed linked with the E domains of TRiC; while in the presence of ATP-AlFx,
242 additional XLs formed with the A/I domains of TRiC (Fig. 3i), indicating an upward
243 shift of tubulin induced by ATP binding and hydrolysis. Indeed, more TRiC A and I
244 domain regions were observed to be involved in the interaction with tubulin in the S2
245 and S3 states (Figs. 2j and 3g) than in the S1 state (Fig. 1h). Inspection of the S2 and
246 S3 maps suggested that ATP-hydrolysis could induce considerable downward rotation
247 of the A and E domains of TRiC from the open to closed state (Extended Data Fig. 7o).
248 These substantial movements could dramatically reduce the chamber volume, and
249 hence restrain the conformational landscape of the substrate and lead to a more
250 stabilized substrate through intimate interactions with the TRiC A/I domains. In the
251 meanwhile, the mechanical force generated from TRiC ring closure could provide extra
252 energy to help the substrate overcome the energy barrier and transform towards the
253 global energy minimum. This may be a general mechanism for TRiC-mediated
254 substrate folding.

255 **Tubulin engages with closed TRiC through both electrostatic and hydrophilic**
256 **interactions**

257 We then inspected the closed TRiC-tubulin-S3 structure to derive the interaction
258 properties between tubulin and TRiC. Here the electrostatic surface property inside the
259 TRiC chamber was observed to be asymmetric, with the CCT6 hemisphere more
260 positively charged and the CCT2 hemisphere relatively negatively charged (Fig. 4a-b),
261 in line with previous reports on yeast and bovine TRiC[21]. Interestingly, the engaged
262 tubulin N/C domains appear negatively charged, complementary with the contacting
263 CCT6 hemisphere (Fig. 4b). This observation was also consistent with our findings that
264 numerous salt bridges formed between TRiC CCT6 hemisphere subunits and tubulin
265 N/C domains (Fig. 3h). The electrostatic surface of the tubulin I domain was found to

266 be not complementary with the related region of TRiC (Fig. 4a-b), consistent with the
267 lack of a strong interaction between them (Fig. 3g, Extended Data Fig. 7l). Taken
268 together, our S3 structure revealed previously unreported strong electrostatic
269 interactions between the tubulin N/C domains and the TRiC CCT6 hemisphere subunits.

270 Inspection of the S3 structure also suggested an enrichment of hydrophilic residues
271 at the interaction interfaces between the TRiC inner dome and tubulin, creating a mostly
272 polar TRiC-tubulin interface in the closed chamber (Fig. 4c). This type of polar
273 interface was also seen in the TRiC-σ3 complex[30]. Taken together, our data suggested
274 that the closed-state TRiC interacts with its obligate substrate tubulin through a
275 combination of electrostatic and hydrophilic interactions to stabilize this substrate and
276 facilitate its folding.

277 We have previously showed that yeast TRiC can close both rings in the presence
278 of natural nucleotide ATP[16]. Here we performed further cryo-EM study on human TRiC
279 incubated with ATP at 1 mM, a physiological concentration of ATP in the cell[16,54], and
280 obtained two maps, including an open-state TRiC and a both-ring-closed TRiC (27.2 %
281 of the population) (Extended Data Fig. 8a-c). The closed TRiC map showed that all
282 nucleotide pockets were occupied, in addition to a tubulin density within one TRiC
283 chamber in a position and orientation similar to that observed in the TRiC-tubulin-S3
284 map (Extended Data Fig. 8d-e). Collectively, these results suggested that the double-
285 closed state for both yeast and human TRiC indeed exists in the presence of natural
286 nucleotide, in line with a recent *in situ* cryo-ET study on neuron cells[55].

287 **Cryo-EM map of TRiC-ADP**

288 To capture the complete TRiC ATPase cycle, we determined a cryo-EM map of
289 TRiC in the presence of ADP to a resolution of 3.3 Å (termed TRiC-ADP, Fig. 5a-b,
290 Extended Data Fig. 1e, 9, and 10a-b). In this map, TRiC is in the open conformation,
291 overall similar to that of TRiC-NPP (Extended Data Fig. 10c), but with all of the
292 subunits loaded with ADP (Fig. 5c, Extended Data Fig. 10d). However, other than the
293 remaining unstructured tail density, there was no engaged tubulin anymore within TRiC
294 chamber (Fig. 5b). Corroborate to this, our XL-MS data showed no detected cross-links

295 between TRiC and tubulin after the ADP incubation (Fig. 5d), indicating that under our
296 experimental condition ADP binding on TRiC could potentially contribute to a release
297 of tubulin from TRiC regardless of tubulin folding status. We performed further 3DVA
298 on the dataset and found TRiC-ADP to be very dynamic, with all the subunits (including
299 the most stable CCT6) displaying outward/inward tilting motions (Extended Data Fig.
300 10e, Supplementary Video 2). We then postulate that the dynamic nature of TRiC-ADP
301 may contribute to the substrate release in this state. Still, we should mention that here
302 we used the TRiC-ADP structure to mimic the state that, after releasing γ-phosphate,
303 TRiC reached the open state and then also released the substrate.

304 **The C- and N-termini of TRiC play distinct roles in substrate folding and TRiC**
305 **allosteric coordination**

306 Here, we showed that in each of the four open-state TRiC structures (TRiC-NPP,
307 S1, S2, and TRiC-ADP), there is a central unstructured tail density between the two
308 equators (Fig. 1e, g, Fig. 2b and Fig. 5b). Moreover, in both the S1 and S2 structures,
309 the resolved portions of the TRiC C-termini and the extended unstructured tail density
310 apparently form contacts with the tubulin substrate and hence potentially stabilize the
311 substrate (Fig. 1g-h and Fig. 2b, j).

312 Strikingly, in the closed TRiC-tubulin-S3 structure, the N-terminus of almost all
313 of the TRiC subunits were stabilized and very well resolved (Extended Data Fig. 11).
314 Specifically, the N-termini of all subunits except CCT4 were observed to contact H1 of
315 the neighboring subunit, and those of CCT2/4/5/7/8 to involve in the inter-ring
316 allosteric network (Extended Data Fig. 11a-g). This observation is consistent with our
317 previous finding in yeast TRiC, suggesting that the extra layer of N-terminal allosteric
318 network could play important roles in TRiC ring closure[16]. Intriguingly, we observed
319 the N-terminus of CCT8' from the trans-ring adopting a bent conformation and
320 extending all the way to the cis-ring to associate with the tubulin N domain (Fig. 4d),
321 in addition to being involved in the inter-ring allosteric network by linking the CCT6/6'
322 N-termini and CCT3 stem loop together. This indicated that CCT8 may play a critical
323 role in substrate stabilization/folding besides being involved in TRiC inter-ring

324 cooperativity.

325 Notably, in the closed S3 state, we also resolved a portion of the C-terminal
326 extensions for most TRiC subunits (except CCT4), and captured the uncharacterized
327 direct interactions between these C-terminal extensions of TRiC and tubulin (Fig. 4e).
328 These C-terminal extensions, mostly hydrophilic (Fig. 4f), stretch out from the
329 surrounding subunits towards the center of TRiC chamber to form physical contacts
330 with tubulin, and hence appearing like a net holding and stabilizing tubulin within the
331 TRiC chamber (Fig. 4e), which may facilitate tubulin folding. Consistent with this,
332 previous studies suggested that the C-termini of GroEL form contacts with its substrate,
333 which could enhance and accelerate substrate folding, and that the hydrophilic residues
334 on the C-termini are critical for substrate folding[56-59].

335 Discussion

336 Tubulin is the building block of the microtubule, which is critical to many cellular
337 processes, and the eukaryotic chaperonin TRiC is required for tubulin biogenesis. Here,
338 we captured snapshots of tubulin folding pathway mediated by TRiC, by acquiring six
339 cryo-EM structures of human TRiC in its ATPase cycle with three of them engaged with
340 endogenous tubulin in different folding stages (Fig. 1, 2, and 5). Importantly, our TRiC-
341 tubulin-S3 structure revealed a near-natively folded tubulin engaged with closed TRiC
342 in one chamber, primarily with the A/I domains of the CCT3/6/8 subunits through
343 electrostatic and hydrophilic interactions (Fig. 4a-c). We also noticed the interaction of
344 TRiC termini with tubulin in the open TRiC-tubulin-S1 and -S2 states (Fig. 1h, 2j), and
345 found that in the closed S3 state the N terminus of CCT8 from the opposite ring and the
346 C-terminal extensions of almost all TRiC subunits may play a role in tubulin
347 stabilization and folding (Fig. 4d-f).

348 Proposed pathway and mechanism of TRiC-mediated tubulin folding

349 Here we propose a complete picture of TRiC-mediated tubulin folding pathway
350 and mechanism conjugated with the ATP-driven conformational cycle of TRiC (Fig.
351 6a). After being translated from ribosomes, nascent tubulin polypeptides are delivered

352 to TRiC by co-chaperon prefoldin to enter its folding pathway associated with the TRiC
353 ATPase cycle[49,60]. Subsequently, tubulin can be released inside TRiC chamber, making
354 contacts with the E domains of all of the TRiC subunits and with the unstructured
355 termini of TRiC, to form the TRiC-tubulin-S1 state, in which the tubulin is relatively
356 dynamic (step 1). After ATP binds to TRiC, with the resulting stabilization of the folding
357 machinery, tubulin can be gradually translocated upwards to associate with the A/I
358 domains of CCT6/8 in addition to keeping contacts with the E domains of all of the
359 subunits (step 2). Once hydrolysis of ATP triggers TRiC ring closure (with the
360 involvement of TRiC N-termini), C-terminal extensions of TRiC and the N-terminus of
361 CCT8 from the opposite ring could stabilize and potentially facilitate the upward
362 translocation of tubulin to result in the formation of intimate electrostatic and
363 hydrophilic interactions between the A domain of CCT6 hemisphere subunits and the
364 N/C domains of tubulin. These directional contacts and constraints on the tubulin N/C
365 domains could facilitate its folding towards the native state, and the mechanical force
366 generated by TRiC ring closure including the considerable downward rotation of the A
367 domain of every TRiC subunit could be propagated to tubulin and drive it to overcome
368 the energy barrier to transform towards the global minimum reaching the folded state
369 (step 3). Subsequently, in the γ-phosphate released open TRiC-ADP state, the associated
370 tubulin could be released from TRiC chamber (step 4). Based on previous reports, the
371 dynamic β-tubulin I domain could then be recognized and capped by cofactor A,
372 followed by the assembly of β-tubulin with α-tubulin into tubulin heterodimers with
373 the assistance of cofactors C, D, and E[61-63]. Finally, the tubulin heterodimers assemble
374 into the microtubule, which goes on to perform its biological functions.

375 **Conformational landscape of TRiC-mediated tubulin folding**

376 Without TRiC-assisted folding, nascent tubulins are prone to form aggregates due
377 to the high energy barrier for spontaneous folding to reach the native folded state[64]. In
378 the current work, by capturing multiple intermediate states of tubulin folding assisted
379 by TRiC, we were able to derive a hypothetical energy landscape of the three distinct
380 states of TRiC-tubulin on the basis of nucleotide binding status, complex stability, and

population distribution (Fig. 6b). In TRiC-tubulin-S1, the engagement with TRiC could potentially stabilize the nascent tubulin, leading it to overcome the first energy barrier to reach a lower level in the energy landscape. Still, the tubulin at this stage remains quite dynamic, accompanying the dynamic nature of TRiC in the NPP state with only CCT3/6/8 subunits preloaded with ADP (Extended Data Fig. 3f-g). The subsequent binding of ATP to all of the TRiC subunits could drive TRiC and associated tubulin to overcome the next barrier and to stabilize in the steadier TRiC-tubulin-S2 state, evidenced by the observation that the engaged tubulin density here becoming further stabilized and appearing larger. Only when ATP-hydrolysis provides sufficient chemical energy to enable TRiC to overcome the final energy barrier, shutting both rings and becoming transformed to the most stable TRiC-tubulin-S3 state, the confined tubulin is now folded to its near native state inside the closed TRiC chamber. This step may be the rate-limiting step in tubulin folding process. Thus, the ATP-mediated gradual stabilization of TRiC guides tubulin along a pathway that avoids deep kinetic traps in the folding energy landscape. That is to say, binding of tubulin to TRiC could lower the folding energy barrier of tubulin and result in its stabilization, so that it eventually reaches its folded state accompanying ATP-driven TRiC ring closure.

Asymmetric working mechanism of TRiC

TRiC subunits have been previously demonstrated to display a gradient of ATP affinities[27], as well as differences in nucleotide binding[15,19,28] and consumption[16], with these features closely related to the structural asymmetry among TRiC subunits[19,24,65]. In the current study, our results further depicted that in the TRiC-NPP state, the bound ADP in CCT3/6/8 may play a role in stabilizing these subunits, making them appear less intrinsically dynamic than the other subunits (Fig. 1d, f). Consequently, CCT3/6/8 may serve as a dock for an initial engagement of tubulin (Fig. 1h and Fig. 2j), and eventually for close electrostatic and hydrophilic contacts with the N/C domains of tubulin in its nearly folded state (Fig. 3h and Fig. 4a-c). Consistently, previous studies also suggested important roles of CCT3/6/8 in the recognition of other substrates such as mLST8, reovirus σ3 capsid protein, and AML1-175[26-28]. Taken together, the

410 asymmetry of TRiC subunits in structural features and nucleotide consumption may
411 contribute to TRiC-assisted substrate folding.

412 In addition, we found that along with the substrate folding, from a relatively
413 disordered state to an ordered state, TRiC also appears to follow a similar trend:
414 transforming from the relatively dynamic and asymmetric open S1 state to the stabilized,
415 rather symmetrical both-ring-closed S3 state. And during this process, the nucleotide
416 occupancy status also appears to change, from an initial partial occupancy in the NPP
417 state to the full occupancy in all the subunits of TRiC, with the nucleotide states
418 becoming more homologous (Extended Data Fig. 3f, 7g-h). In the nucleotide binding
419 and consumption, as well as ring closure, the asymmetric machinery—TRiC displays a
420 stepwise mechanism[16,19] rather than a concerted manner as in the Group I system[66,67].
421 As has been suggested previously[68], the asymmetry or non-concerted nature of TRiC in
422 the open state could be beneficial for its ability to recognize and engage with diverse
423 substrates. Moreover, despite that our study and most other studies revealed only one
424 substrate engaged with TRiC[7,11,28,29,69,70], there was a crystal structure showing that
425 TRiC can simultaneously bind two tubulins, one per ring[15], implying two substrates
426 could interact with a TRiC complex simultaneously at least under certain physiological
427 conditions[68] and both rings of TRiC may have the ability to perform substrate folding
428 concurrently for efficient protein quality control under these conditions.

429 In summary, our study depicted a thorough picture of the pathway and
430 conformational landscape of TRiC-mediated tubulin folding accompanying the ATPase
431 cycle of the folding machinery. Furthermore, our determination of the interaction sites
432 between tubulin and the closed TRiC chamber is beneficial for the development of
433 novel and effective therapeutic agents specifically targeting TRiC-tubulin interactions.

434 ## Methods

435 **Purification of human TRiC**. Human TRiC was purified from HEK293F cells
436 according to the published protocol with some modifications[28,49,71]. Briefly, the pellet
437 was lysed with iced MQA-10% glycerol buffer (50 mM NaCl, 20 mM Hepes pH 7.4, 5
438 mM $MgCl_2$, 1 mM DTT, 10% glycerol, 1 mM PMSF, and 2 mM ATP) using one
439 Protease Inhibitor Cocktail Tablet (Roche) per 100 mL of the lysate. The lysed material
440 was then subjected to centrifugation (20,000 g for 30 min to remove cellular debris and
441 nuclei and then 140,000 g for 1.5 h to remove the ribosome) in order to separate the
442 cytoplasmic fraction. The resulting supernatant was filtered using a 0.44 μm filter
443 membrane, and then passed through a Q Sepharose column (GE Healthcare). TRiC was
444 eluted in a gradient from 40 to 80% MQB-5% glycerol (MQA with 1 M NaCl). The
445 fractions containing TRiC were pooled, diluted with MQA to ensure an NaCl
446 concentration of about 100 mM, and applied to a Heparin HiTrap HP column (GE
447 Healthcare). TRiC was eluted in a gradient from 20 to 65% MQB-5% glycerol. The
448 fractions containing TRiC were pooled and incubated with 10 mM ATP on a shaker
449 (220 rpm, 37 °C，30 min) to allow TRiC to cycle and release substrate before
450 performing gel filtration chromatography (GFC). The sample was then concentrated
451 down to 0.5 mL and loaded onto a Superose 6 Increase 10/300 GL column (GE
452 Healthcare) with MQA-5% glycerol without ATP. TRiC eluted at about 13-15.5 mL of
453 the size-exclusion column, consistent with that of a 1-MDa complex. Finally, the
454 sample was subjected multiple times to buffer exchange to remove remaining ATP in
455 the buffer, and we obtained biologically active TRiC (Extended Data Fig. 1a-b).

456 It is noteworthy that TRiC-mediated folding of tubulin is associated with release
457 of predominantly nonnative forms of tubulin from chaperonin, and with the majority of
458 released tubulin requiring further rounds of binding/release to reach its native state[72].
459 This indicates the released nonnative substrate could re-bind on TRiC to go through
460 further round of ATPase cycle. In our experimental condition, it is possible that the
461 tubulin in TRiC-tubulin-S1 has already gone through one or several ATPase cycles.

462 **ATPase activity assay**. The ATP hydrolysis rate of TRiC was measured by performing

463 an NADH-coupled assay[73]. In this assay, each ATP hydrolysis event allows for a
464 conversion of one molecule of phosphoenolpyruvate into pyruvate catalyzed by
465 pyruvate kinase, with pyruvate then converted to lactate by L-lactate dehydrogenase,
466 which results in oxidation of a single NADH molecule. Loss of NADH over time, a
467 measure quantifiably proportional to the ATP hydrolysis rate, was monitored in the
468 current work by measuring the decrease in absorbance of light at a wavelength of 340
469 nm. All of the assays were conducted at room temperature in a buffer containing 10
470 mM HEPES/NaOH pH 7.5, 50 mM NaCl, and 10 mM $MgCl_2$, in the presence of 1 mM
471 ATP. Experiments were performed in triplicate using 0.3 μM of the protein complex.
472 Absorbance was measured in a 200 μl reaction volume using a 96-well plate reader.
473 Data analysis was performed using Graph Pad Prism 8.

474 **ADP/ATP ratio assay.** To identify the form of the nucleotide in our purified human
475 TRiC, we carried out luciferin-luciferase reactions with an ADP/ATP ratio assay kit[74]
476 (Sigma-Aldrich). To release the bound nucleotide from TRiC for measurement, the
477 TRiC sample was first digested with proteinase K, according to a previously published
478 protocol[75] with minor modifications. TRiC proteolytic-digestion experiments were
479 carried out by adding a 1 μl aliquot of 2 mg/ml proteinase K to a 19 μl aliquot of 4.5
480 mg/ml TRiC in dilution buffer (20 mM Hepes-KOH pH 7.4, 50 mM NaCl, 5 mM $MgCl_2$,
481 1 mM DTT, and 5% glycerol). The digestion was performed at 37 °C for 1 h. The
482 reactions were then terminated by adding PMSF (to a final concentration of 5 mM) into
483 the reaction mixture and waiting for 10 minutes. Afterwards, the nucleotide form in the
484 TRiC sample was identified by using the ADP/ATP ratio assay kit according to the
485 manufacturer's protocol, and the RLU values of ATP and ADP were measured with a
486 Synergy Neo2 multimode reader (BioTek).

487 **Cross-linking and mass spectrometry analysis**. The purified TRiC was cross-linked
488 by using bis[sulfosuccinimidyl] suberate (BS^3) (Sigma), with a spacer arm of 11.4 Å
489 between their Cα carbons, on ice for 2 hours. The final concentration of the crosslinker
490 was 2 mM. The reaction was then terminated by using 50 mM Tris-HCl pH 7.5 at room
491 temperature for 15 minutes. For the sample containing ATP-AlFx, the purified TRiC

492 was incubated with 1 mM ATP, 5 mM $MgCl_2$, 5 mM $Al(NO_3)_3$, and 30 mM NaF for 1
493 h at 37 °C, and the resulting product was cross-linked by using BS^3 following the above-
494 mentioned conditions. Cross-linked complexes were precipitated and digested for 16
495 hours at 37 °C by using trypsin at an enzyme-to-substrate ratio of 1:50 (w/w). The
496 tryptic-digested peptides were desalted and loaded on an in-house packed capillary
497 reverse-phase C18 column (length of 40 cm, 100 µm ID x 360 µm OD, 1.9 µm particle
498 size, pore diameter of 120 Å) connected to an Easy LC 1200 system. The samples were
499 analyzed with a 120 min-HPLC gradient of 6% to 35% of buffer B (buffer A: 0.1%
500 formic acid in Water; buffer B: 0.1% formic acid in 80% acetonitrile) at 300 nL/minute.
501 The eluted peptides were ionized and directly introduced into a Q-Exactive mass
502 spectrometer using a nano-spray source. Survey full-scan MS spectra (from m/z 300–
503 1800) were acquired using an Orbitrap analyzer with a resolution r=70,000 at an m/z of
504 400. Cross-linked peptides were identified and evaluated using pLink2 software[76].

505 **Cryo-EM sample preparation.** To prepare the vitrified sample of TRiC, the purified
506 TRiC was diluted to 1.2 mg/ml, and an aliquot of 2 µl of this sample was applied onto
507 a plasma cleaned holey carbon grid (Quantifoil, R1.2/1.3, 200 mesh). The grid was
508 blotted with Vitrobot Mark IV (Thermo Fisher Scientific) and then plunged into liquid
509 ethane cooled by liquid nitrogen. To prepare the sample of TRiC in the presence of 1
510 mM ATP-AlFx, the purified TRiC was diluted to 1.2 mg/ml, and incubated with 1 mM
511 ATP, 5 mM $MgCl_2$, 5 mM Al $(NO_3)_3$, and 30 mM NaF at 37 °C for 1 h prior to freezing.
512 To prepare the sample of TRiC with 1 mM ADP, the purified TRiC was diluted to 1.2
513 mg/ml, and incubated with 1 mM ADP and 5 mM $MgCl_2$ at 37 °C for 1 h prior to
514 freezing. Moreover, to prepare the sample of TRiC in the presence of 1 mM ATP, the
515 purified TRiC was diluted to 1.2 mg/ml, and incubated with 1 mM ATP and 5 mM
516 $MgCl_2$ at 37 °C for 30 s before freezing. We then followed the above-mentioned
517 procedure to prepare the vitrified sample in each case.

518 **Data acquisition**. For each of the experimental sample conditions mentioned above
519 except for TRiC-ATP dataset, cryo-EM movies of the sample were collected using a
520 Titan Krios electron microscope (Thermo Fisher Scientific) operated at an accelerating

521 voltage of 300 kV with a nominal magnification of 18,000x (yielding a pixel size of
522 1.318 Å, Table 1). The movies were recorded on a K2 Summit direct electron detector
523 (Gatan) operated in the super-resolution mode under low-dose condition in an
524 automatic manner using SerialEM[77]. The exposure time for each frame was 0.2 s and
525 the total accumulation time was 7.6 s, leading to a total accumulated dose of 38 $e^-/Å^2$
526 on the specimen. For TRiC-ATP dataset, the movies were collected in a magnification
527 of 81,000x (yielding a pixel size of 0.89 Å, Table 1) utilizing a K3 direct electron
528 detector (Gatan) operated in the counting mode under a low-dose condition in an
529 automatic manner using EPU (Thermo Fisher Scientific). Each frame was exposed for
530 0.05 s, and the total accumulation time was 2 s, leading to a total accumulated dose of
531 50 $e^-/Å^2$ on the specimen.

532 **Image processing and 3D reconstruction.** We performed single-particle analysis
533 mainly using Relion 3.1[78,79] unless otherwise specified (Table 1). All images were
534 aligned and summed using MotionCor2[80]. After CTF parameter determination using
535 CTFFIND4[81], particle auto-picking, manual particle checking, and reference-free 2D
536 classification, particles with TRiC features were remained for further processing.

537 For the TRiC sample before addition of nucleotides, 761,665 particles were picked
538 from the original micrographs, and after 2D classification, 709,192 particles remained
539 (Extended Data Fig. 2a). These particles were subjected to 3D refinement, and then
540 were re-extracted and re-centered using the refinement coordinates. After one round of
541 no-align 3D classification and another round of 3D classification, we then combined
542 the substrate-containing particles (including class 1 from the first round and class 3
543 from the second round) together, and performed another round of 3D classification,
544 generating a substrate-containing class with 169,098 particles. After carrying out CTF
545 refinement and polishing on these particles, we obtained a map with weak substrate
546 density at 4.0-Å-resolution. We subtracted the substrate density and performed a no-
547 align 3D classification, and a good class with 68.4% of the particles were reverted to
548 the original particles. We then performed a local refinement on these particles and
549 reconstructed a 4.1-Å-resolution TRiC-tubulin-S1 map displaying better substrate

density. For the substrate-free class 4 particles from the second round of 3D classification, we performed another round of 3D classification, resulting in a better class having 185,216 particles. After CTF refinement and Bayesian polishing, these particles were refined to a 3.1-Å-resolution TRiC-NPP map. The resolution estimation was based on the gold-standard Fourier Shell Correlation (FSC) criterion of 0.143.

For the dataset of TRiC in the presence of ATP-AlFx, after 2D classification, 544,809 particles remained (Extended Data Fig. 5a). These particles were subjected to 3D classification. The particles from class 4, displaying closed-state features, were subjected to another round of 3D classification and a resulting better class with 168,472 particles was further refined to produce a 2.9-Å-resolution map with weak substrate density inside the TRiC chamber. Thus, we focused on the extra density inside the chamber and performed a no-align 3D classification, generating 4 classes. Particles from classes 1 and 2, appearing to have tubulin density, were combined (total of 103,406 particles) and refined to produce a 3.1-Å-resolution TRiC-tubulin-S3 map; class 3 (62,412 particles), having an extra tail density, were used to reconstruct a 3.2-Å-resolution TRiC-ADP-AlFx map. In addition, particles of classes 1-3 from the first round of 3D classification were subjected to another round of 3D classification and yielded a better class with 98,046 particles that were refined to produce a 4.3-Å-resolution map. Through focused refinement and focused classification, we eventually obtained a 4.2-Å-resolution map with tubulin density in one ring, termed TRiC-tubulin-S2.

For the dataset of TRiC-ADP, after 2D classification, 344,486 and 319,306 particles remained for dataset 1 and 2, respectively (Extended Data Fig. 9a). After refinement and re-centering, the particles were further cleaned in cryoSPARC through 2D classification and heterogeneous refinement. Then the good particles were subjected to two rounds of 3D classification in Relion 3.1. Subsequently, the better-resolved classes 3/4 from dataset 1 and classes 2/3 from dataset 2 were combined and subjected to one more round of 3D classification. The better class with 239,315 particles were further refined to a 3.3-Å-resolution TRiC-ADP map.

579 For the TRiC-ATP dataset, after 2D classification 225,085 particles remained
580 (Extended Data Fig. 8a). These particles were refined and re-extracted, and further
581 cleaned up in cryoSPARC by 2D classification and heterogeneous refinement to yield
582 three classes. Class 1 open-state particles were subjected to another round of
583 heterogeneous refinement, and the 111,413 particles of the better class 1 were refined
584 to produce a 3.8-Å-resolution TRiC-ATP-open map. Closed-state particles from class 2
585 of the first round of heterogeneous refinement were subjected to another round of
586 heterogeneous refinement, and particles from the better class 2 were refined in Relion
587 3.1 to produce a 4.5-Å-resolution TRiC-ATP-closed map.

588 **Model building by flexible fitting**. We built the homology models for human TRiC in
589 the open and closed states and for tubulin (TUBB5) using the SWISS-MODEL server[82],
590 with the cryo-EM structures of the yeast TRiC in the open and closed conformations
591 (PDB ID: 5GW4, 5GW5, 6KS6[16,19]) and the cryo-EM structure of human TUBB3
592 tubulin (PDB ID: 5JCO[83]) as templates, respectively. Afterwards, we refined the model
593 against the corresponding cryo-EM map using Rossetta[84], and then Phenix[85].
594 Furthermore, to improve the fitting between model and map, we performed real-space
595 refinement using COOT[86]. Finally, we used Phenix again for the last round of flexible
596 fitting of the entire complex.

597 We used UCSF Chimera and ChimeraX for generating figures and performing
598 electrostatic surface property calculations[87,88]. Interaction surface analysis was
599 conducted by using the PISA server[89].

Acknowledgements

We are grateful to the staffs of the NCPSS Electron Microscopy facility, Database and Computing facility, Mass Spectrometry facility, and Protein Expression and Purification facility for instrumental support and technical assistance. This work was supported by grants from the Strategic Priority Research Program of CAS (XDB37040103), the National Basic Research Program of China (2017YFA0503503), the NSFC (32130056, 31670754 and 31872714), the Shanghai Academic Research Leader (20XD1404200), Shanghai Pilot Program for Basic Research–CAS, Shanghai Branch (JCYJ-SHFY-2022-008), and the CAS Facility-based Open Research Program.

Author contributions

Y.C. and C.L. designed the experiments. C.L. purified the proteins and performed functional analysis with the involvement of Q.Z.. C.L. and M.J. with the involvement of S.W. and W.H. collected the cryo-EM data. C.L. with the involvement of C.X. and Y-F. Wang performed data reconstruction and model building. Y-X. Wang, L.D., and L.B. helped supervise the functional analysis. C.P., C.L., and Y.Y. performed the XL-MS analysis. Y.C. and C.L. analyzed the structure and wrote the manuscript.

Data availability

All data presented in this study are available within the figures and in the Supplementary Information. Cryo-EM maps and the associated models have been deposited in the EMDB and Protein Data Bank, respectively, with the accession ID as the following: TRiC-NPP (EMDB-32922, PDB-7X0A), TRiC-tubulin-S1 (EMDB-32903, PDB-7WZ3), TRiC-tubulin-S2 (EMDB-32989, PDB-7X3J), TRiC-tubulin-S3 (EMDB-32923, PDB-7X0S), TRiC-ADP-AlFx (EMDB-32926, PDB-7X0V), TRiC-ADP (EMDB-32993, PDB-7X3U), TRiC-ATP-closed (EMDB-33025, PDB-7X6Q), TRiC-ATP-open (EMDB-33053, PDB-7X7Y).

Competing interests

The authors declare no competing interests.

Reference

1 Tam, S. *et al.* The chaperonin TRiC blocks a huntingtin sequence element that promotes the conformational switch to aggregation. *Nature Structural & Molecular Biology* **16**, 1279-U1298, doi:10.1038/nsmb.1700 (2009).

2 Khabirova, E. *et al.* The TRiC/CCT chaperone is implicated in Alzheimer's disease based on patient GWAS and an RNAi screen in Abeta-expressing Caenorhabditis elegans. *PLoS One* **9**, e102985, doi:10.1371/journal.pone.0102985 (2014).

3 Pereira, J. H. *et al.* Mechanism of nucleotide sensing in group II chaperonins. *EMBO J* **31**, 731-740, doi:10.1038/emboj.2011.468 (2012).

4 Hayer-Hartl, M., Bracher, A. & Hartl, F. U. The GroEL-GroES Chaperonin Machine: A Nano-Cage for Protein Folding. (2016).

5 Balchin, D., Hayer-Hartl, M. & Hartl, F. U. In vivo aspects of protein folding and quality control. *Science* **353**, aac4354, doi:10.1126/science.aac4354 (2016).

6 Joachimiak, L. A., Walzthoeni, T., Liu, C. W., Aebersold, R. & Frydman, J. The structural basis of substrate recognition by the eukaryotic chaperonin TRiC/CCT. *Cell* **159**, 1042-1055, doi:10.1016/j.cell.2014.10.042 (2014).

7 Balchin, D., Milicic, G., Strauss, M., Hayer-Hartl, M. & Hartl, F. U. Pathway of Actin Folding Directed by the Eukaryotic Chaperonin TRiC. *Cell* **174**, 1507-1521 e1516, doi:10.1016/j.cell.2018.07.006 (2018).

8 Llorca, O. *et al.* Eukaryotic type II chaperonin CCT interacts with actin through specific subunits. *Nature* **402**, 693-696, doi:Doi 10.1038/45294 (1999).

9 Llorca, O. *et al.* Eukaryotic chaperonin CCT stabilizes actin and tubulin folding intermediates in open quasi-native conformations. *Embo Journal* **19**, 5971-5979, doi:DOI 10.1093/emboj/19.22.5971 (2000).

10 Camasses, A., Bogdanova A Fau - Shevchenko, A., Shevchenko A Fau - Zachariae, W. & Zachariae, W. The CCT chaperonin promotes activation of the anaphase-promoting complex through the generation of functional Cdc20. (2003).

11 Plimpton, R. L. *et al.* Structures of the Gbeta-CCT and PhLP1-Gbeta-CCT complexes reveal a mechanism for G-protein beta-subunit folding and Gbetagamma dimer assembly. *Proc Natl Acad Sci U S A* **112**, 2413-2418, doi:10.1073/pnas.1419595112 (2015).

12 Kasembeli, M. *et al.* Modulation of STAT3 folding and function by TRiC/CCT chaperonin. *PLoS Biol* **12**, e1001844, doi:10.1371/journal.pbio.1001844 (2014).

13 Trinidad, A. G. *et al.* Interaction of p53 with the CCT complex promotes protein folding and wild-type p53 activity. *Mol Cell* **50**, 805-817, doi:10.1016/j.molcel.2013.05.002 (2013).

14 McClellan, A. J., Scott Md Fau - Frydman, J. & Frydman, J. Folding and quality control of the VHL tumor suppressor proceed through distinct chaperone pathways. (2005).

15 Munoz, I. G. *et al.* Crystal structure of the open conformation of the mammalian chaperonin CCT in complex with tubulin. *Nat Struct Mol Biol* **18**, 14-19, doi:10.1038/nsmb.1971 (2011).

16 Jin, M. *et al.* An ensemble of cryo-EM structures of TRiC reveal its conformational landscape and subunit specificity. *Proc Natl Acad Sci U S A* **116**, 19513-19522, doi:10.1073/pnas.1903976116 (2019).

17 Kalisman, N., Adams, C. M. & Levitt, M. Subunit order of eukaryotic TRiC/CCT chaperonin by cross-linking, mass spectrometry, and combinatorial homology modeling. *Proc Natl Acad Sci U*

670 *S A* **109**, 2884-2889, doi:10.1073/pnas.1119472109 (2012).
671 18 Wang, H., Han, W., Takagi, J. & Cong, Y. Yeast Inner-Subunit PA–NZ-1 Labeling Strategy for
672 Accurate Subunit Identification in a Macromolecular Complex through Cryo-EM Analysis.
673 *Journal of Molecular Biology* **430**, 1417-1425, doi:https://doi.org/10.1016/j.jmb.2018.03.026
674 (2018).
675 19 Zang, Y. *et al.* Staggered ATP binding mechanism of eukaryotic chaperonin TRiC (CCT) revealed
676 through high-resolution cryo-EM. *Nat Struct Mol Biol* **23**, 1083-1091, doi:10.1038/nsmb.3309
677 (2016).
678 20 Zang, Y. *et al.* Development of a yeast internal-subunit eGFP labeling strategy and its
679 application in subunit identification in eukaryotic group II chaperonin TRiC/CCT. *Sci Rep* **8**, 2374,
680 doi:10.1038/s41598-017-18962-y (2018).
681 21 Leitner, A. *et al.* The molecular architecture of the eukaryotic chaperonin TRiC/CCT. *Structure*
682 **20**, 814-825, doi:10.1016/j.str.2012.03.007 (2012).
683 22 Booth, C. R. *et al.* Mechanism of lid closure in the eukaryotic chaperonin TRiC/CCT. *Nat Struct*
684 *Mol Biol* **15**, 746-753, doi:10.1038/nsmb.1436 (2008).
685 23 Cong, Y. *et al.* 4.0-A resolution cryo-EM structure of the mammalian chaperonin TRiC/CCT
686 reveals its unique subunit arrangement. *Proc Natl Acad Sci U S A* **107**, 4967-4972,
687 doi:10.1073/pnas.0913774107 (2010).
688 24 Cong, Y. *et al.* Symmetry-free cryo-EM structures of the chaperonin TRiC along its ATPase-
689 driven conformational cycle. *EMBO J* **31**, 720-730, doi:10.1038/emboj.2011.366 (2012).
690 25 Meyer, A. S. *et al.* Closing the folding chamber of the eukaryotic chaperonin requires the
691 transition state of ATP hydrolysis. *Cell* **113**, 369-381, doi:10.1016/s0092-8674(03)00307-6
692 (2003).
693 26 Liu, C. *et al.* Cryo-EM study on the homo-oligomeric ring formation of yeast TRiC/CCT subunits
694 reveals TRiC ring assembly mechanism. *BioRxiv*, doi:10.1101/2021.02.24.432666 (2021).
695 27 Reissmann, S. *et al.* A gradient of ATP affinities generates an asymmetric power stroke driving
696 the chaperonin TRIC/CCT folding cycle. *Cell Rep* **2**, 866-877, doi:10.1016/j.celrep.2012.08.036
697 (2012).
698 28 Cuellar, J. *et al.* Structural and functional analysis of the role of the chaperonin CCT in mTOR
699 complex assembly. *Nat Commun* **10**, 2865, doi:10.1038/s41467-019-10781-1 (2019).
700 29 Roh, S. H., Kasembeli, M. M., Galaz-Montoya, J. G., Chiu, W. & Tweardy, D. J. Chaperonin
701 TRiC/CCT Recognizes Fusion Oncoprotein AML1-ETO through Subunit-Specific Interactions.
702 *Biophys J* **110**, 2377-2385, doi:10.1016/j.bpj.2016.04.045 (2016).
703 30 Knowlton, J. J. *et al.* Structural and functional dissection of reovirus capsid folding and assembly
704 by the prefoldin-TRiC/CCT chaperone network. *Proceedings of the National Academy of*
705 *Sciences* **118**, e2018127118, doi:10.1073/pnas.2018127118 (2021).
706 31 Llorca, O. *et al.* Analysis of the interaction between the eukaryotic chaperonin CCT and its
707 substrates actin and tubulin. *J Struct Biol* **135**, 205-218, doi:10.1006/jsbi.2001.4359 (2001).
708 32 Llorca, O. *et al.* The 'sequential allosteric ring' mechanism in the eukaryotic chaperonin-
709 assisted folding of actin and tubulin. *EMBO J* **20**, 4065-4075, doi:10.1093/emboj/20.15.4065
710 (2001).
711 33 Jin, M., Liu, C., Han, W. & Cong, Y. in *Macromolecular Protein Complexes II: Structure and*
712 *Function* (eds J. Robin Harris & Jon Marles-Wright) 625-654 (Springer International Publishing,
713 2019).

714 34 Leroux, M. R. & Hartl, F. U. Protein folding: Versatility of the cytosolic chaperonin TRIC/CCT.
715 *Current Biology* **10**, R260-R264, doi:Doi 10.1016/S0960-9822(00)00432-2 (2000).
716 35 Ursic, D. & Culbertson, M. R. The Yeast Homolog to Mouse Tcp-1 Affects Microtubule-Mediated
717 Processes. *Molecular and Cellular Biology* **11**, 2629-2640, doi:Doi 10.1128/Mcb.11.5.2629
718 (1991).
719 36 Yaffe, M. B. *et al.* TCP1 complex is a molecular chaperone in tubulin biogenesis. *Nature* **358**,
720 245-248, doi:10.1038/358245a0 (1992).
721 37 Sternlicht, H. *et al.* The t-complex polypeptide 1 complex is a chaperonin for tubulin and actin
722 in vivo. *Proceedings of the National Academy of Sciences of the United States of America* **90**,
723 9422-9426, doi:10.1073/pnas.90.20.9422 (1993).
724 38 Sullivan, K. F. Structure and Utilization of Tubulin Isotypes. *Annual Review of Cell Biology* **4**, 687-
725 716, doi:10.1146/annurev.cb.04.110188.003351 (1988).
726 39 Breuss, M. *et al.* Mutations in the β-tubulin gene TUBB5 cause microcephaly with structural
727 brain abnormalities. *Cell reports* **2**, 1554-1562, doi:10.1016/j.celrep.2012.11.017 (2012).
728 40 Poirier, K. *et al.* Mutations in the neuronal β-tubulin subunit TUBB3 result in malformation of
729 cortical development and neuronal migration defects. *Human Molecular Genetics* **19**, 4462-
730 4473, doi:10.1093/hmg/ddq377 (2010).
731 41 Tischfield, M. A. *et al.* Human TUBB3 Mutations Perturb Microtubule Dynamics, Kinesin
732 Interactions, and Axon Guidance. *Cell* **140**, 74-87, doi:10.1016/j.cell.2009.12.011 (2010).
733 42 Ballatore, C., Lee, V. M. & Trojanowski, J. Q. Tau-mediated neurodegeneration in Alzheimer's
734 disease and related disorders. *Nat Rev Neurosci* **8**, 663-672, doi:10.1038/nrn2194 (2007).
735 43 Nogales, E. & Alushin, G. M. Tubulin and Microtubule Structure: Mechanistic Insights Into
736 Dynamic Instability and Its Biological Relevance doi:10.1016/b978-0-12-809633-8.08056-0
737 (2017).
738 44 Lin, Y. F., Tsai, W. P., Liu, H. G. & Liang, P. H. Intracellular beta-tubulin/chaperonin containing
739 TCP1-beta complex serves as a novel chemotherapeutic target against drug-resistant tumors.
740 *Cancer Res* **69**, 6879-6888, doi:10.1158/0008-5472.CAN-08-4700 (2009).
741 45 Liu, Y. J., Kumar, V., Lin, Y. F. & Liang, P. H. Disrupting CCT-beta : beta-tubulin selectively kills CCT-
742 beta overexpressed cancer cells through MAPKs activation. *Cell Death Dis* **8**, e3052,
743 doi:10.1038/cddis.2017.425 (2017).
744 46 Chen, J. *et al.* Cryo-EM of mammalian PA28alphabeta-iCP immunoproteasome reveals a
745 distinct mechanism of proteasome activation by PA28alphabeta. *Nat Commun* **12**, 739,
746 doi:10.1038/s41467-021-21028-3 (2021).
747 47 Chaudhry, C., Horwich, A. L., Brunger, A. T. & Adams, P. D. Exploring the structural dynamics of
748 the E.coli chaperonin GroEL using translation-libration-screw crystallographic refinement of
749 intermediate states. *J Mol Biol* **342**, 229-245, doi:10.1016/j.jmb.2004.07.015 (2004).
750 48 Clare, D. K. *et al.* ATP-triggered conformational changes delineate substrate-binding and -
751 folding mechanics of the GroEL chaperonin. *Cell* **149**, 113-123, doi:10.1016/j.cell.2012.02.047
752 (2012).
753 49 Gestaut, D. *et al.* The Chaperonin TRiC/CCT Associates with Prefoldin through a Conserved
754 Electrostatic Interface Essential for Cellular Proteostasis. *Cell* **177**, 751-765 e715,
755 doi:10.1016/j.cell.2019.03.012 (2019).
756 50 Cuellar, J. *et al.* The Molecular Chaperone CCT Sequesters Gelsolin and Protects it from
757 Cleavage by Caspase-3. *J Mol Biol* **434**, 167399, doi:10.1016/j.jmb.2021.167399 (2021).

758 51 Punjani, A. & Fleet, D. J. 3D variability analysis: Resolving continuous flexibility and discrete
759 heterogeneity from single particle cryo-EM. *J Struct Biol* **213**, 107702,
760 doi:10.1016/j.jsb.2021.107702 (2021).
761 52 You, L., Gillilan, R. & Huffaker, T. C. Model for the yeast cofactor A-beta-tubulin complex based
762 on computational docking and mutagensis. *Journal of Molecular Biology* **341**, 1343-1354,
763 doi:10.1016/j.jmb.2004.06.081 (2004).
764 53 Kelly, J. J. *et al.* Snapshots of actin and tubulin folding inside the TRiC chaperonin. *Nat Struct*
765 *Mol Biol*, doi:10.1038/s41594-022-00755-1 (2022).
766 54 Huang, H. B. *et al.* Physiological levels of ATP negatively regulate proteasome function. *Cell*
767 *Research* **20**, 1372-1385, doi:10.1038/cr.2010.123 (2010).
768 55 Guo, Q. *et al.* In Situ Structure of Neuronal C9orf72 Poly-GA Aggregates Reveals Proteasome
769 Recruitment. *Cell* **172**, 696-705 e612, doi:10.1016/j.cell.2017.12.030 (2018).
770 56 Machida, K., Kono-Okada, A., Hongo, K., Mizobata, T. & Kawata, Y. Hydrophilic residues 526
771 KNDAAD 531 in the flexible C-terminal region of the chaperonin GroEL are critical for substrate
772 protein folding within the central cavity. *J Biol Chem* **283**, 6886-6896,
773 doi:10.1074/jbc.M708002200 (2008).
774 57 Ishino, S. *et al.* Effects of C-terminal Truncation of Chaperonin GroEL on the Yield of In-cage
775 Folding of the Green Fluorescent Protein. *J Biol Chem* **290**, 15042-15051,
776 doi:10.1074/jbc.M114.633636 (2015).
777 58 Chen, D. H. *et al.* Visualizing GroEL/ES in the act of encapsulating a folding protein. *Cell* **153**,
778 1354-1365, doi:10.1016/j.cell.2013.04.052 (2013).
779 59 Weaver, J. *et al.* GroEL actively stimulates folding of the endogenous substrate protein PepQ.
780 *Nat Commun* **8**, 15934, doi:10.1038/ncomms15934 (2017).
781 60 Hansen, W. J., Cowan, N. J. & Welch, W. J. Prefoldin-nascent chain complexes in the folding of
782 cytoskeletal proteins. *Journal of Cell Biology* **145**, 265-277, doi:DOI 10.1083/jcb.145.2.265
783 (1999).
784 61 Gao, Y., Vainberg, I. E., Chow, R. L. & Cowan, N. J. Two cofactors and cytoplasmic chaperonin
785 are required for the folding of alpha- and beta-tubulin. *Mol Cell Biol* **13**, 2478-2485,
786 doi:10.1128/mcb.13.4.2478-2485.1993 (1993).
787 62 Grynberg, M., Jaroszewski, L. & Godzik, A. Domain analysis of the tubulin cofactor system: a
788 model for tubulin folding and dimerization. *BMC Bioinformatics* **4**, 46, doi:10.1186/1471-2105-
789 4-46 (2003).
790 63 Tian, G. *et al.* Pathway Leading to Correctly Folded β-Tubulin. *Cell* **86**, 287-296,
791 doi:10.1016/S0092-8674(00)80100-2 (1996).
792 64 Hartl, F. U., Bracher, A. & Hayer-Hartl, M. Molecular chaperones in protein folding and
793 proteostasis. *Nature* **475**, 324-332, doi:10.1038/nature10317 (2011).
794 65 Rivenzon-Segal, D., Wolf, S. G., Shimon, L., Willison, K. R. & Horovitz, A. Sequential ATP-induced
795 allosteric transitions of the cytoplasmic chaperonin containing TCP-1 revealed by EM analysis.
796 *Nat Struct Mol Biol* **12**, 233-237, doi:10.1038/nsmb901 (2005).
797 66 Ma, J. P., Sigler, P. B., Xu, Z. H. & Karplus, M. A dynamic model for the allosteric mechanism of
798 GroEL. *Journal of Molecular Biology* **302**, 303-313, doi:10.1006/jmbi.2000.4014 (2000).
799 67 Horovitz, A. & Willison, K. R. Allosteric regulation of chaperonins. *Curr Opin Struc Biol* **15**, 646-
800 651, doi:10.1016/j.sbi.2005.10.001 (2005).
801 68 Yebenes, H., Mesa, P., Munoz, I. G., Montoya, G. & Valpuesta, J. M. Chaperonins: two rings for

802 folding. *Trends Biochem Sci* **36**, 424-432, doi:10.1016/j.tibs.2011.05.003 (2011).
803 69 Dekker, C. *et al.* The crystal structure of yeast CCT reveals intrinsic asymmetry of eukaryotic
804 cytosolic chaperonins. *EMBO J* **30**, 3078-3090, doi:10.1038/emboj.2011.208 (2011).
805 70 Knowlton, J. J. *et al.* Structural and functional dissection of reovirus capsid folding and assembly
806 by the prefoldin-TRiC/CCT chaperone network. *Proc Natl Acad Sci U S A* **118**,
807 doi:10.1073/pnas.2018127118 (2021).
808 71 Knee, K. M., Sergeeva, O. A. & King, J. A. Human TRiC complex purified from HeLa cells contains
809 all eight CCT subunits and is active in vitro. *Cell Stress Chaperones* **18**, 137-144,
810 doi:10.1007/s12192-012-0357-z (2013).
811 72 Farr, G. W., Scharl, E. C., Schumacher, R. J., Sondek, S. & Horwich, A. L. Chaperonin-mediated
812 folding in the eukaryotic cytosol proceeds through rounds of release of native and nonnative
813 forms. *Cell* **89**, 927-937, doi:10.1016/s0092-8674(00)80278-0 (1997).
814 73 Norby, J. G. Coupled Assay of Na+,K+-Atpase Activity. *Method Enzymol* **156**, 116-119 (1988).
815 74 Polletta, L. *et al.* SIRT5 regulation of ammonia-induced autophagy and mitophagy. *Autophagy*
816 **11**, 253-270, doi:10.1080/15548627.2015.1009778 (2015).
817 75 Szpikowska, B. K., Swiderek Km Fau - Sherman, M. A., Sherman Ma Fau - Mas, M. T. & Mas, M.
818 T. MgATP binding to the nucleotide-binding domains of the eukaryotic cytoplasmic chaperonin
819 induces conformational changes in the putative substrate-binding domains. (1998).
820 76 Lu, S. *et al.* Mapping native disulfide bonds at a proteome scale. *Nature Methods* **12**, 329-U373,
821 doi:10.1038/Nmeth.3283 (2015).
822 77 Mastronarde, D. N. Automated electron microscope tomography using robust prediction of
823 specimen movements. *Journal of Structural Biology* **152**, 36-51, doi:10.1016/j.jsb.2005.07.007
824 (2005).
825 78 Scheres, S. H. W. Semi-automated selection of cryo-EM particles in RELION-1.3. *Journal of*
826 *structural biology* **189**, 114-122, doi:10.1016/j.jsb.2014.11.010 (2015).
827 79 Fernandez-Leiro, R. & Scheres, S. H. W. A pipeline approach to single-particle processing in
828 RELION. *Acta Crystallographica Section D-Structural Biology* **73**, 496-502,
829 doi:10.1107/S2059798316019276 (2017).
830 80 Zheng, S. Q. *et al.* MotionCor2: anisotropic correction of beam-induced motion for improved
831 cryo-electron microscopy. *Nature methods* **14**, 331-332, doi:10.1038/nmeth.4193 (2017).
832 81 Rohou, A. & Grigorieff, N. CTFFIND4: Fast and accurate defocus estimation from electron
833 micrographs. *J Struct Biol* **192**, 216-221, doi:10.1016/j.jsb.2015.08.008 (2015).
834 82 Arnold, K., Bordoli, L., Kopp, J. & Schwede, T. The SWISS-MODEL workspace: a web-based
835 environment for protein structure homology modelling. *Bioinformatics* **22**, 195-201,
836 doi:10.1093/bioinformatics/bti770 (2006).
837 83 Vemu, A. *et al.* Structure and Dynamics of Single-isoform Recombinant Neuronal Human
838 Tubulin. *Journal of Biological Chemistry* **291**, 12907-12915, doi:10.1074/jbc.C116.731133
839 (2016).
840 84 DiMaio, F. *et al.* Atomic-accuracy models from 4.5-A cryo-electron microscopy data with
841 density-guided iterative local refinement. *Nature methods* **12**, 361-365,
842 doi:10.1038/nmeth.3286 (2015).
843 85 Adams, P. D. *et al.* PHENIX: a comprehensive Python-based system for macromolecular
844 structure solution. *Acta Crystallogr D* **66**, 213-221, doi:10.1107/S0907444909052925 (2010).
845 86 Emsley, P. & Cowtan, K. Coot: model-building tools for molecular graphics. *Acta*

Crystallographica Section D-Biological Crystallography **60**, 2126-2132, doi:10.1107/S0907444904019158 (2004).

87 Pettersen, E. F. *et al.* UCSF chimera - A visualization system for exploratory research and analysis. *J Comput Chem* **25**, 1605-1612, doi:10.1002/jcc.20084 (2004).

88 Goddard, T. D. *et al.* UCSF ChimeraX: Meeting modern challenges in visualization and analysis. *Protein Science* **27**, 14-25, doi:10.1002/pro.3235 (2018).

89 Schlee, S. *et al.* Prediction of quaternary structure by analysis of hot spot residues in protein-protein interfaces: the case of anthranilate phosphoribosyltransferases. *Proteins* **87**, 815-825, doi:10.1002/prot.25744 (2019).

856 **FIGURES**

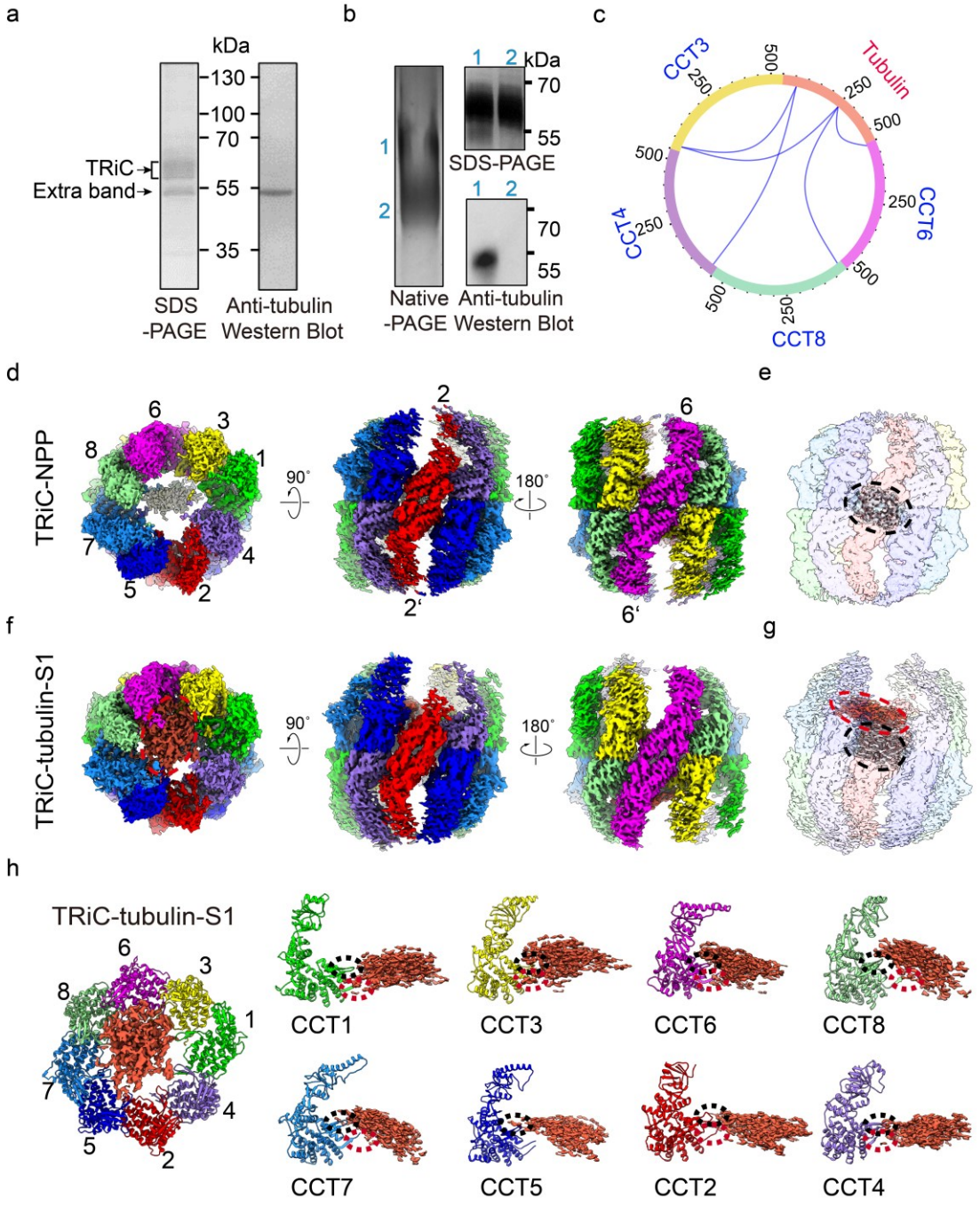

857

858 **Fig. 1 | Cryo-EM structures of the endogenously purified TRiC with associated**
859 **tubulin. a**, Sodium dodecyl sulfate-polyacrylamide gel electrophoresis (SDS-PAGE)
860 of the endogenous human TRiC purified from HEK293F cells. This gel suggested the
861 presence of an extra associated protein at ~50 kDa, which was proved to be tubulin by
862 Western blot. **b**, Native gel analysis of TRiC, showing two bands, labeled as 1 and 2,
863 which were excised and loaded into SDS-PAGE. SDS-PAGE analysis suggested that
864 both bands contain TRiC oligomer, and there is an additional band in lane 1, which

865 contained tubulin, as shown by Western blot. **c**, XL-MS analysis of the endogenously
866 purified TRiC with associated tubulin. Identified cross-linked TRiC-tubulin contacts
867 are shown as blue lines. **d,** End-on and side views of TRiC-NPP, with the different
868 subunits in different colors and labeled. This subunit color scheme is followed in
869 subsequent figures. **e,** The unstructured N- and C-terminal tail density (in grey,
870 indicated by a black dashed ellipsoid) of TRiC subunits located between the two
871 equators in TRiC-NPP (transparent density). **f-g,** Cryo-EM map of TRiC-tubulin-S1 (**f**),
872 revealing extra density (shown in red and indicated by a red dashed ellipsoid) within
873 the cis-ring chamber of TRiC (**g**). **h**, Overall binding location of tubulin (red density)
874 in the cis-ring of TRiC-tubulin-S1 (colored ribbon) (left), and the association of tubulin
875 with the E domain of every TRiC subunit, including the C-terminus (indicated by dotted
876 red ellipsoid) and stem loop (dotted black ellipsoid) (right panels).

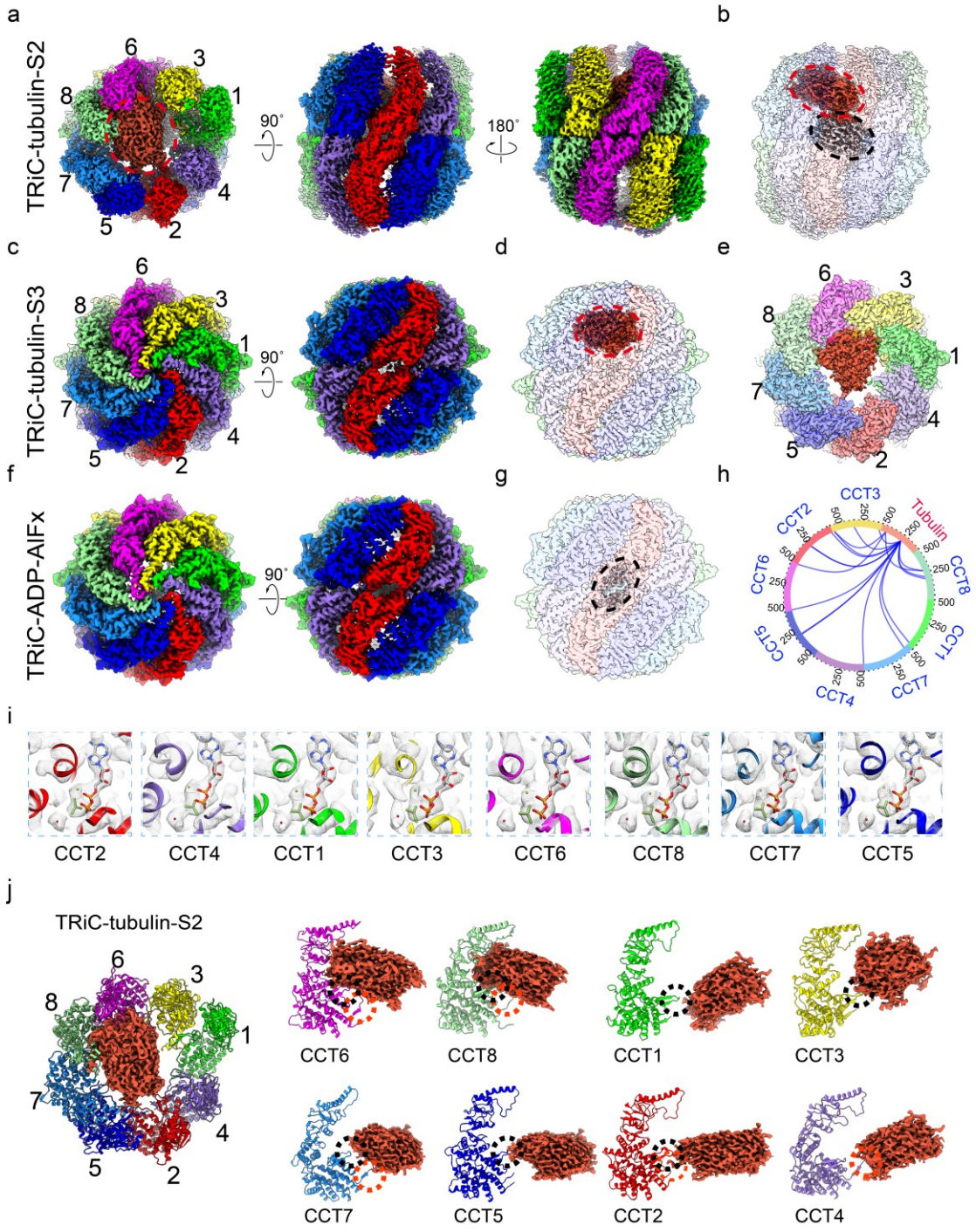

Fig. 2 | Cryo-EM structures of TRiC-tubulin in the presence of ATP-AlFx. **a-b,** Cryo-EM map of TRiC-tubulin-S2 in the open ATP-binding state (**a**), revealing a tail density (in grey) between the two equators and a tubulin density (in red) in the cis-ring of TRiC (transparent density) (**b**). The tail density contacts the tubulin density. **c-d,** Cryo-EM map of TRiC-tubulin-S3 in the closed ATP-hydrolysis transition state (**c**), revealing tubulin density in the cis-ring chamber of TRiC (**d**). **e**, Top view of the TRiC-tubulin-S3 map with TRiC A domains omitted for easier visualization, showing the

885 bound tubulin density, and indicating tubulin mainly associate with CCT6 hemisphere
886 subunits (CCT1/3/6/8). **f-g,** Cryo-EM map of TRiC-ADP-AlFx (**f**), revealing a C-
887 termini mass (black dashed ellipsoid) (**g**), related to Extended Data Fig. 5f. **h**, XL-MS
888 analysis of TRiC with endogenously associated tubulin in the presence of ATP-AlFx. **i**,
889 Portions of the TRiC-tubulin-S3 map in the nucleotide pocket region. All of the subunits
890 bound with ADP-AlFx (stick model) and a magnesium ion (green ball), as well as a
891 water molecule (red ball) in an attacking position, suggesting that all eight subunits are
892 in the ATP-hydrolysis transition state. **j**, Overall binding of tubulin (red density) in the
893 cis-ring of the open TRiC-tubulin-S2. Tubulin was observed to contact all three
894 domains of CCT6/8 and loosely contact the E domains, including the C terminus (dotted
895 red ellipsoid) and stem loop (dotted black ellipsoid), of the remaining subunits.

896

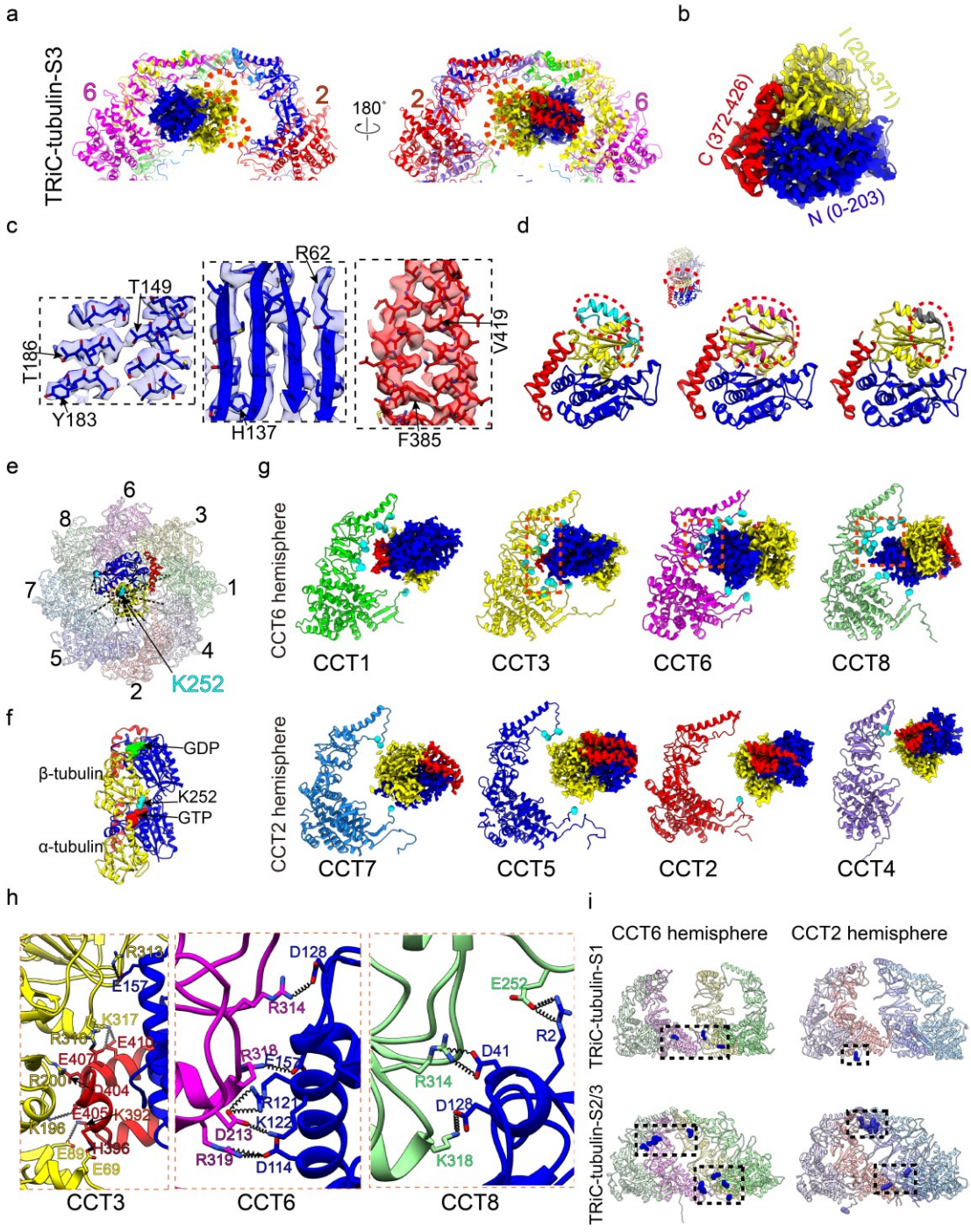

Fig. 3 | TRiC-tubulin-S3 structure showing a near-natively folded tubulin attached to the cis-ring of TRiC. **a**, Enlarged views of the engaged tubulin within the TRiC chamber in the S3 state. The tubulin N/I/C domains are rendered in blue, yellow and red, respectively, which color scheme was followed throughout. Red dotted circles indicate dynamic regions of the I domain of tubulin. **b-c**, The resolved β-tubulin inside the cis-ring of TRiC-tubulin-S3 (**b**), and its high-resolution structural features (**c**). **d**, Ribbon diagram depictions showing the unresolved dynamic portion of the tubulin I

905 domain (in cyan, left) overlapping with its interaction interface with α-tubulin (in violet
906 red, a distance cutoff of 4 Å, middle) or the interaction site with cofactor A (in gray,
907 right)[52]. **e**, Mapping of the detected XLs made by tubulin K58 and K252 (cyan spheres)
908 with the TRiC subunits in the cis-ring of TRiC-tubulin-S3. Note that every TRiC
909 subunit made at least one such XL. **f**, Ribbon diagram illustrating the αβ-tubulin dimer
910 structure, with β-tubulin facing upwards. K252 in β-tubulin and bound nucleotides are
911 shown as spheres. **g**, Ribbon diagram depictions of the association between each TRiC
912 subunit and tubulin in S3, showing the close associations of the N/C domains of tubulin
913 with CCT6 hemisphere subunits CCT1/3/6/8, and loose associations of the tubulin I
914 domain with CCT2 hemisphere subunits CCT7/5/2/4. Cα atoms of the TRiC amino
915 acid residues within 4 Å distance with tubulin are shown as cyan balls. **h**, Magnified
916 views of the regions indicated with red dotted frames in **g** to show the salt bridge
917 interactions formed between tubulin and the CCT3/6/8 subunits. **i**, XL-MS-analysis-
918 derived sites on TRiC (blue spheres) crosslinked with tubulin and mapped onto the
919 corresponding indicated TRiC structure. This analysis suggested a shift in the
920 interaction locations induced by ATP binding/hydrolysis.

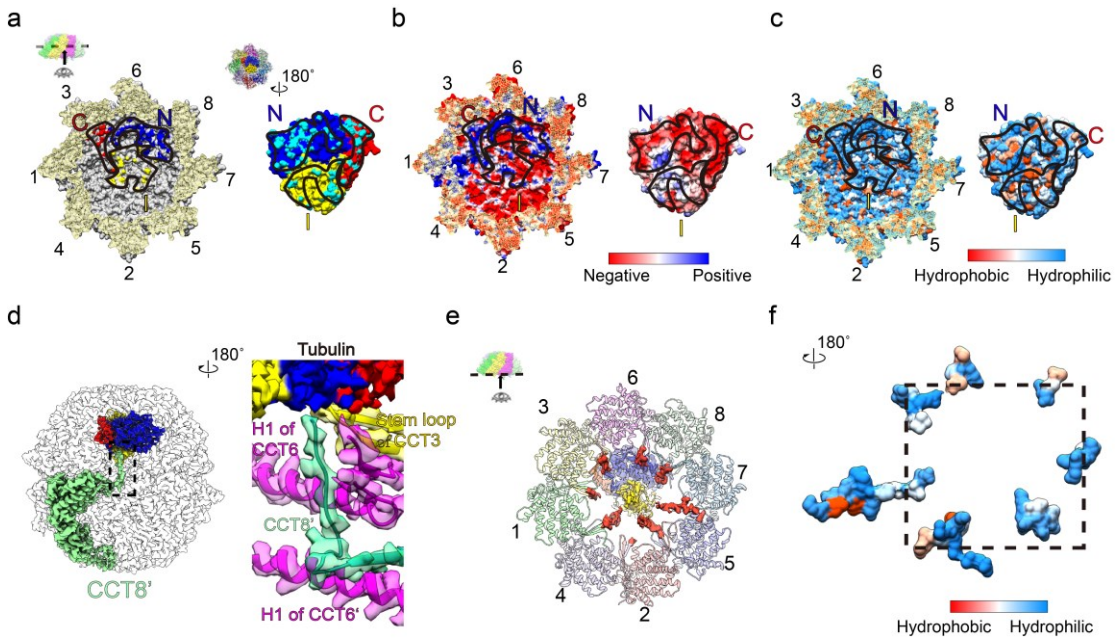

Fig. 4 | Engagement of tubulin with TRiC through electrostatic and hydrophilic interactions, and the roles of TRiC termini in tubulin folding in TRiC-tubulin-S3. **a**, Interaction interface between TRiC and tubulin. The visualization direction and region are shown in the inset. The contact surface residues of TRiC within 4 Å distance of the N/C/I domains of tubulin are colored in blue, red, and yellow, respectively (left panel, black outlines indicate the tubulin footprint on the TRiC interior cavity wall). The contact surface residues of tubulin in proximity to TRiC are colored in cyan (right panel, black outlines indicate the TRiC footprint on the tubulin structure). **b**, An electrostatic surface property analysis, suggesting complementary electrostatic interaction between the CCT3/6/8 subunits of TRiC (mainly positively charged) and the N/C domains of tubulin (mostly negatively charged). **c**, The hydrophilicity/hydrophobicity analysis between TRiC and tubulin, suggesting a hydrophilic interaction between them. **d**, Magnified view of the interaction network of the CCT8' N-terminus. **e**, Depiction showing those resolved portion of C-termini (red density) for all TRiC subunits (besides CCT4) were observed to form contacts with tubulin (central transparent density). **f**, Depiction of the hydrophilicity/hydrophobicity of the resolved C-termini of TRiC, showing these termini to be enriched in hydrophilic residues.

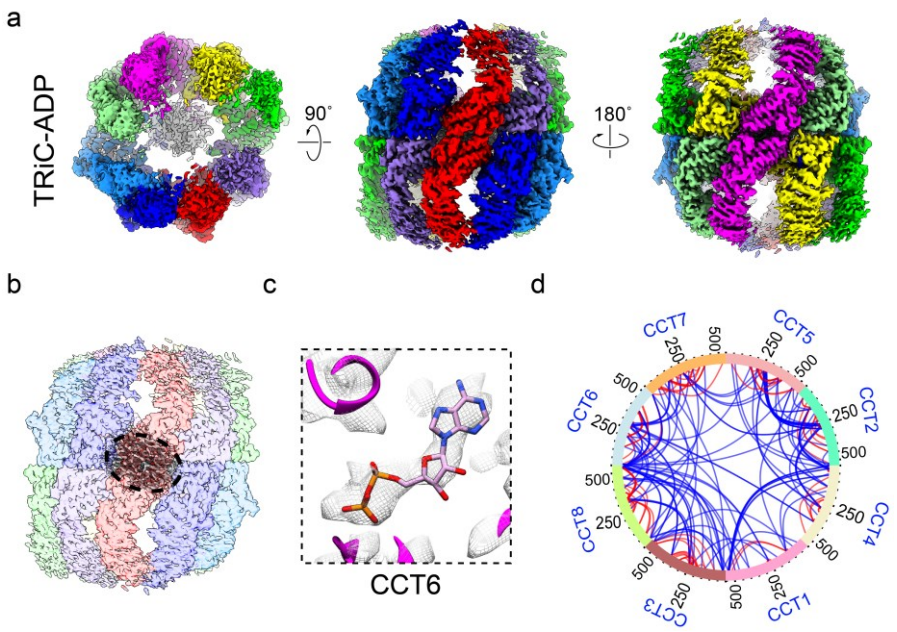

940

941 **Fig. 5 | Cryo-EM and XL-MS analyses of TRiC in the presence of ADP**. **a-b**, Cryo-
942 EM map of TRiC-ADP (**a**), showing the tail density (in grey) remained but substrate
943 released (**b**). **c**, Representative nucleotide density (in the ADP state) of CCT6 in TRiC-
944 ADP. **d**, The XL-MS data showing no cross-links were detected between TRiC and
945 tubulin after ADP incubation. Identified intra-subunit XLs are in red, and inter-subunit
946 XLs in blue.

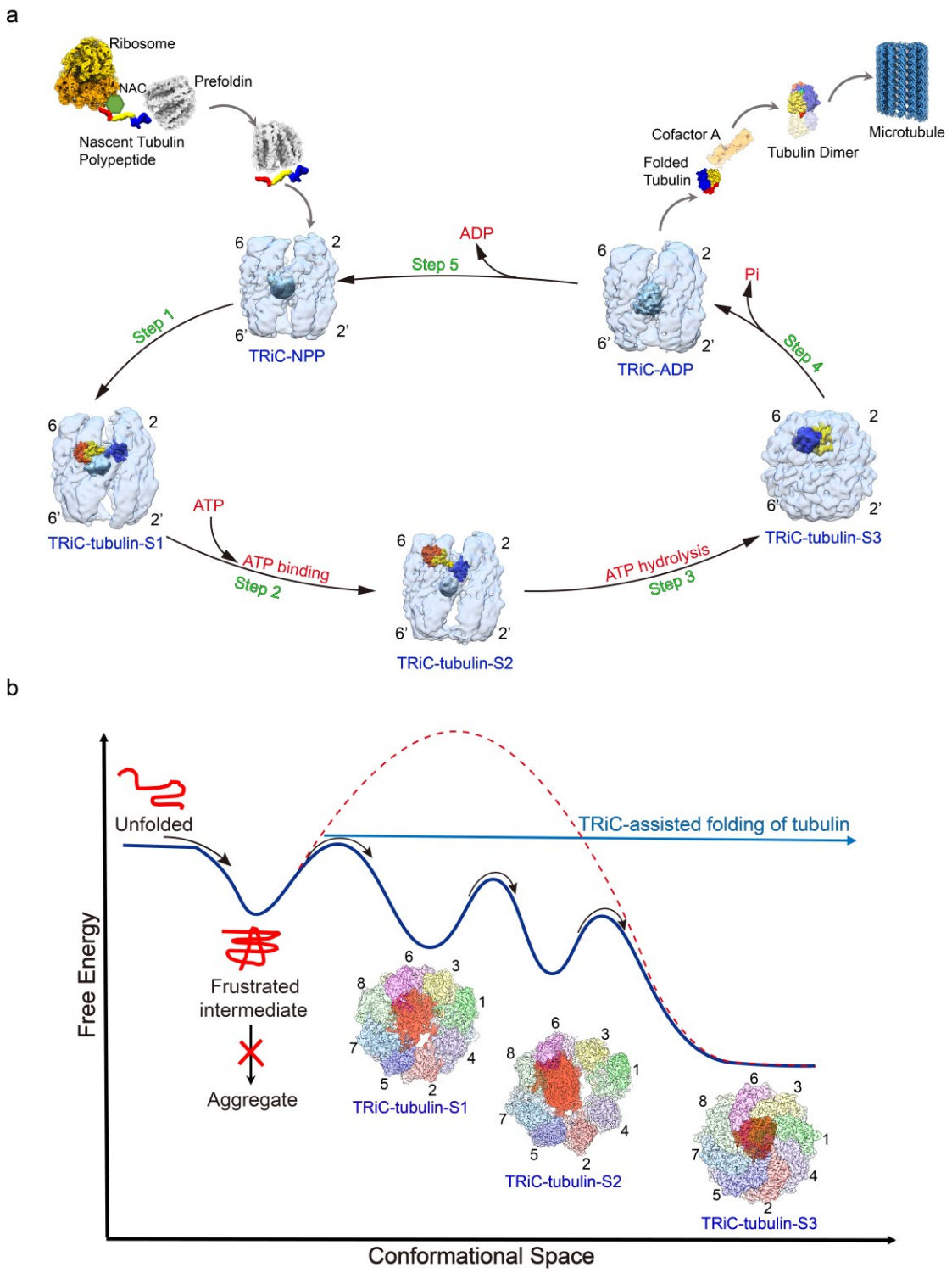

Fig. 6 | The proposed pathway and mechanism of TRiC-mediated tubulin folding. **a**, The proposed pathway of tubulin folding mediated by TRiC associating with its ATP-driven conformational cycle. After being translated from ribosome, nascent tubulin polypeptides are delivered to TRiC-NPP by co-chaperon prefoldin. TRiC is shown in transparent light blue, with its unstructured termini in sky blue density and CCT2/6

being labeled. Tubulin is then released inside the TRiC chamber, contacting with the E domains of all TRiC subunits and with the unstructured termini of TRiC, to form the TRiC-tubulin-S1 state (step 1). After ATP binding to TRiC, tubulin can gradually translocate upwards to associate with the A/I domains of CCT6/8 in addition to keeping contacts with the E domains, forming the TRiC-tubulin-S2 state (step 2). Once ATP-hydrolysis triggers TRiC ring closure, forming the TRiC-tubulin-S3 state, the generated mechanical force together with the directional contacts and constraints on tubulin could facilitate tubulin folding towards the native state (step 3). Subsequently, in the γ-phosphate released open TRiC-ADP state, the associated tubulin could be released from TRiC chamber (step 4). The dynamic β-tubulin I domain could be capped by cofactor A, then assembled with α-tubulin into tubulin heterodimers. Finally, the tubulin heterodimers assemble into the microtubule. TRiC could then release ADP to resume to the NPP state (step 5). All TRiC maps were low passed to 8 Å for easier visualization. **b**, Hypothetical energy landscape of tubulin folding assisted by TRiC. Without TRiC assistance, nascent tubulin is prone to form aggregates or needs to overcome a high energy barrier to achieve its native state. Engagement of tubulin with TRiC in a manner associated with the TRiC ATPase cycle could potentially confine the energy landscape of tubulin and lower its energy barrier, resulting in stabilization of tubulin and finally becoming folded into a substantially near-native state.

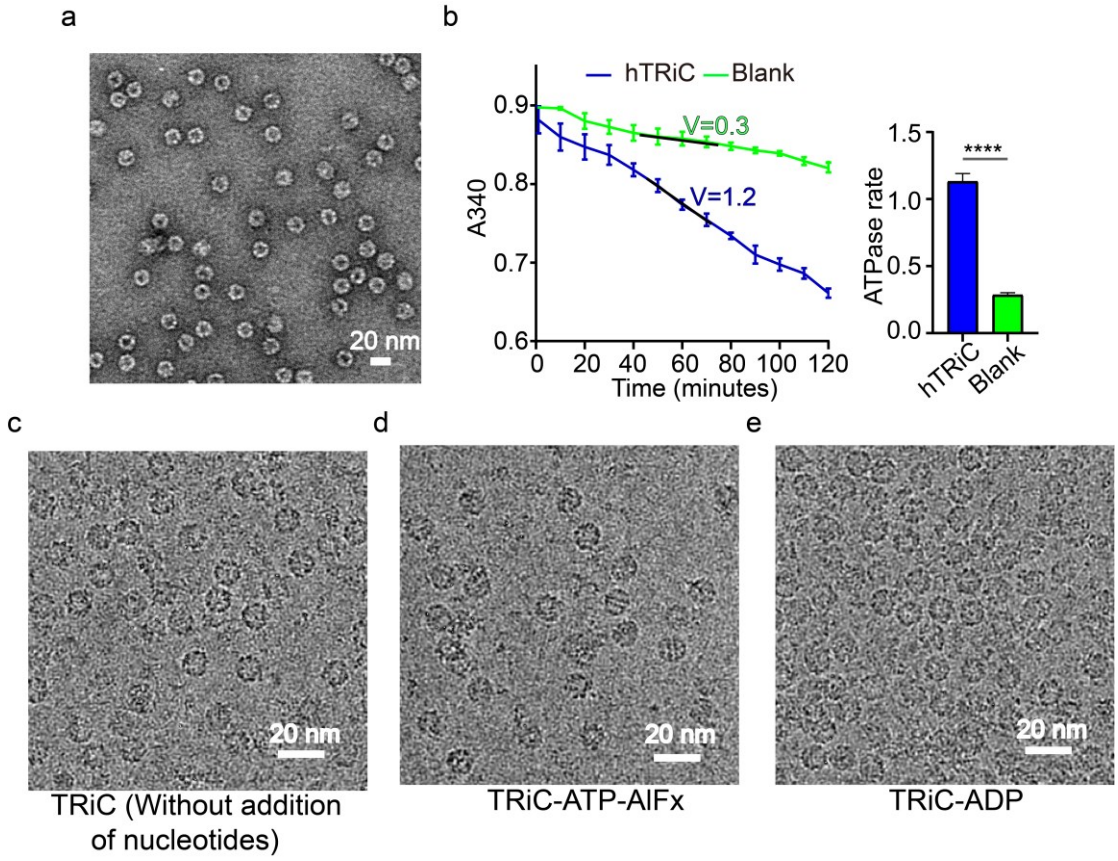

Extended Data Fig. 1 | Human TRiC purified from HEK293F cells. a, Representative negative-stain EM image of purified TRiC. **b**, NADH-coupled enzymatic assays of our purified TRiC and a blank (TRiC buffer without proteins). The results revealed that TRiC was biologically active and could hydrolyze ATP. The ATPase rates (V, with unit of "mole ATP/ [mole TRiC • min]") determined by fitting the linear part of the ATP hydrolysis reaction curves are also provided. An analysis of the significance of the difference between the results (right) suggested that the TRiC sample showed a significantly higher ATPase activity than did the blank, with a statistical significance of ****$P < 0.0001$. For all quantifications, data were plotted as mean ± SD for three independent replicates. **c-e**, Representative cryo-EM images of TRiC sample before adding nucleotides (**c**), in the presence of ATP-AlFx (**d**), and in the presence of ADP (**e**).

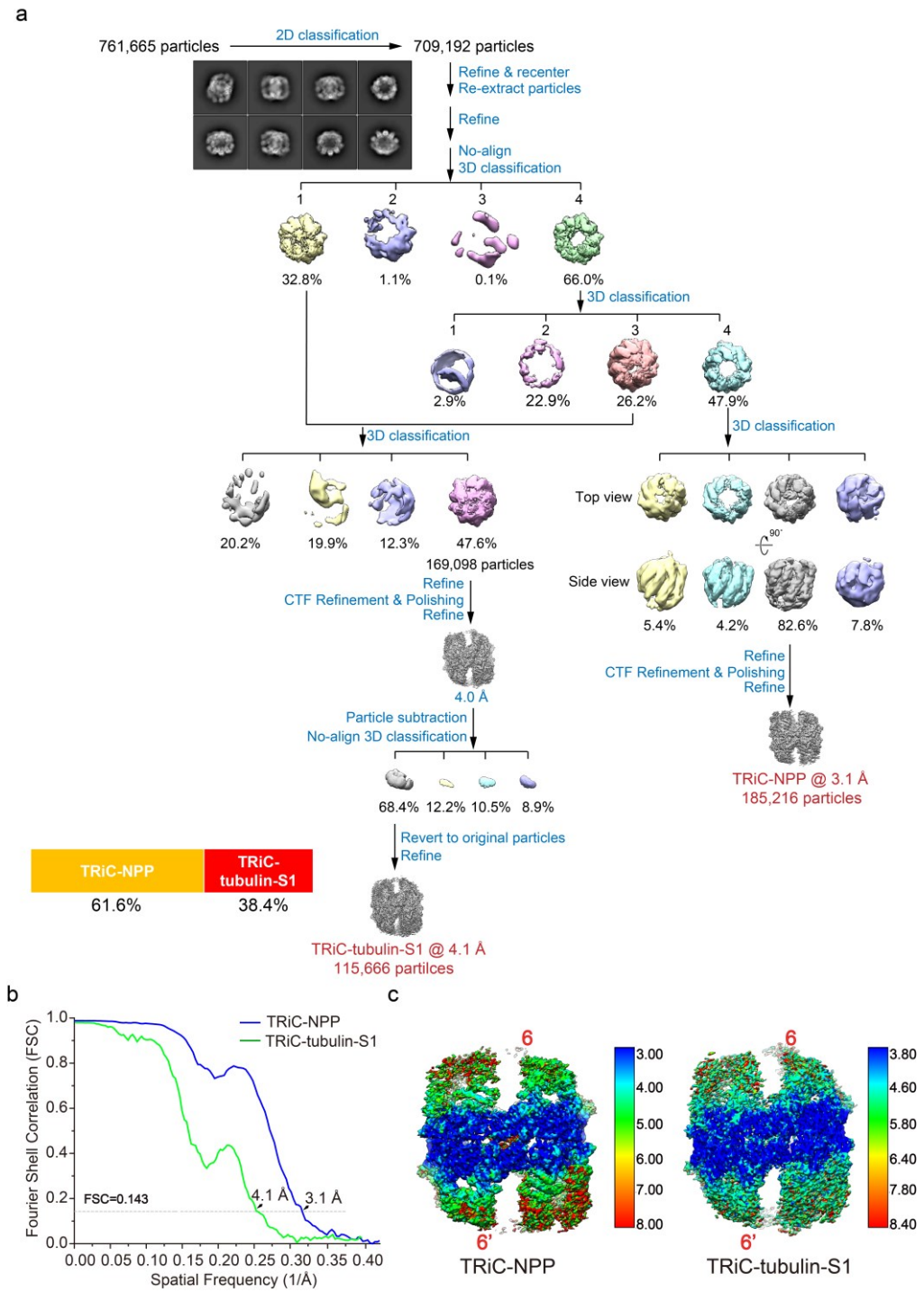

Extended Data Fig. 2 | Work flow for the processing of the cryo-EM data of endogenously purified TRiC. a, Procedure used to process the TRiC cryo-EM data. The reference-free 2D class averages and population distributions of TRiC-NPP and TRiC-tubulin-S1 are also presented. **b-c**, Resolution estimations for TRiC-NPP and TRiC-tubulin-S1 according to the gold-standard FSC criterion of 0.143 (**b**), and local resolution evaluations (**c**).

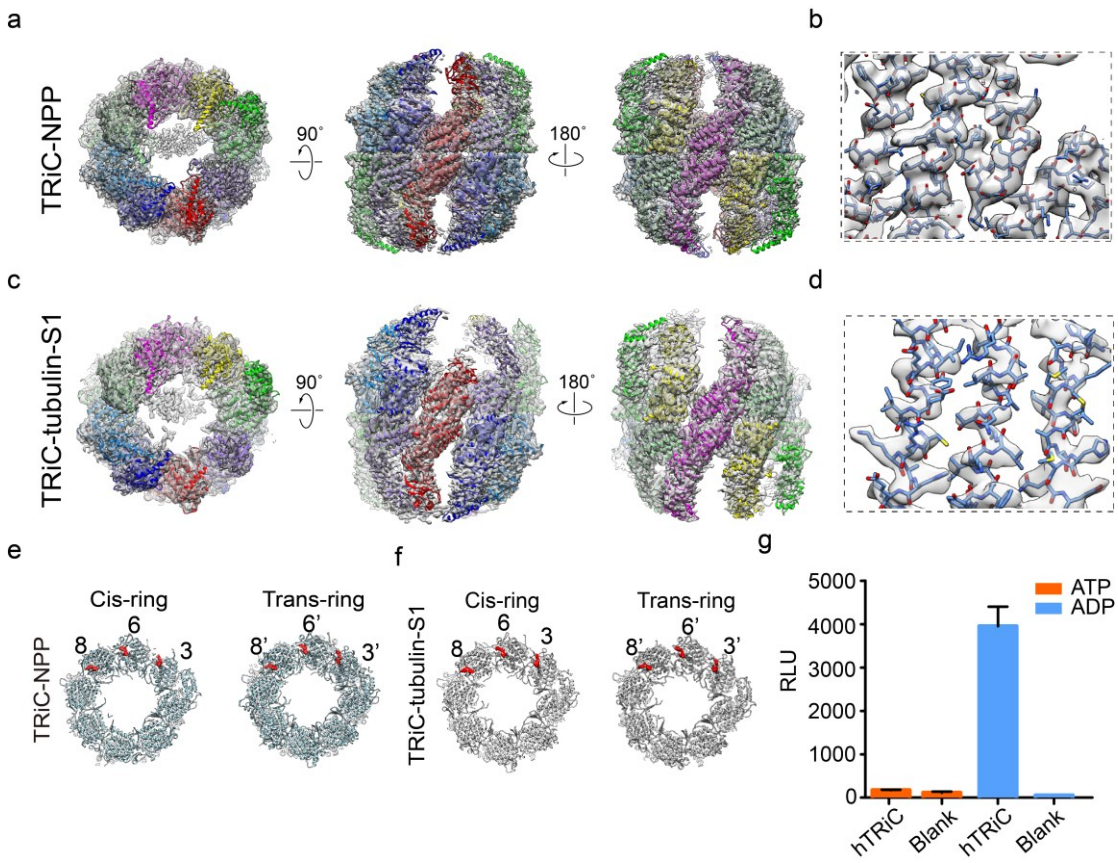

Extended Data Fig. 3 | Atomic models of TRiC-NPP and TRiC-tubulin-S1. **a,c,** Atomic models of TRiC-NPP (**a**) and TRiC-tubulin-S1 (**c**) match well with the corresponding cryo-EM maps. **b,d,** Representative high-resolution structural features of TRiC-NPP (**b**) and TRiC-tubulin-S1 (**d**). **e-f**, Nucleotide occupancy statuses of TRiC-NPP (**e**) and TRiC-tubulin-S1 (**f**), with CCT3/6/8 from both rings having nucleotide density (in red) in their nucleotide pockets. **g**, ATP/ADP ratio analysis of TRiC. The relative light unit (RLU) values were measured for the sample with TRiC buffer as a blank. For all quantifications, data were plotted as mean ± SD for three independent replicates.

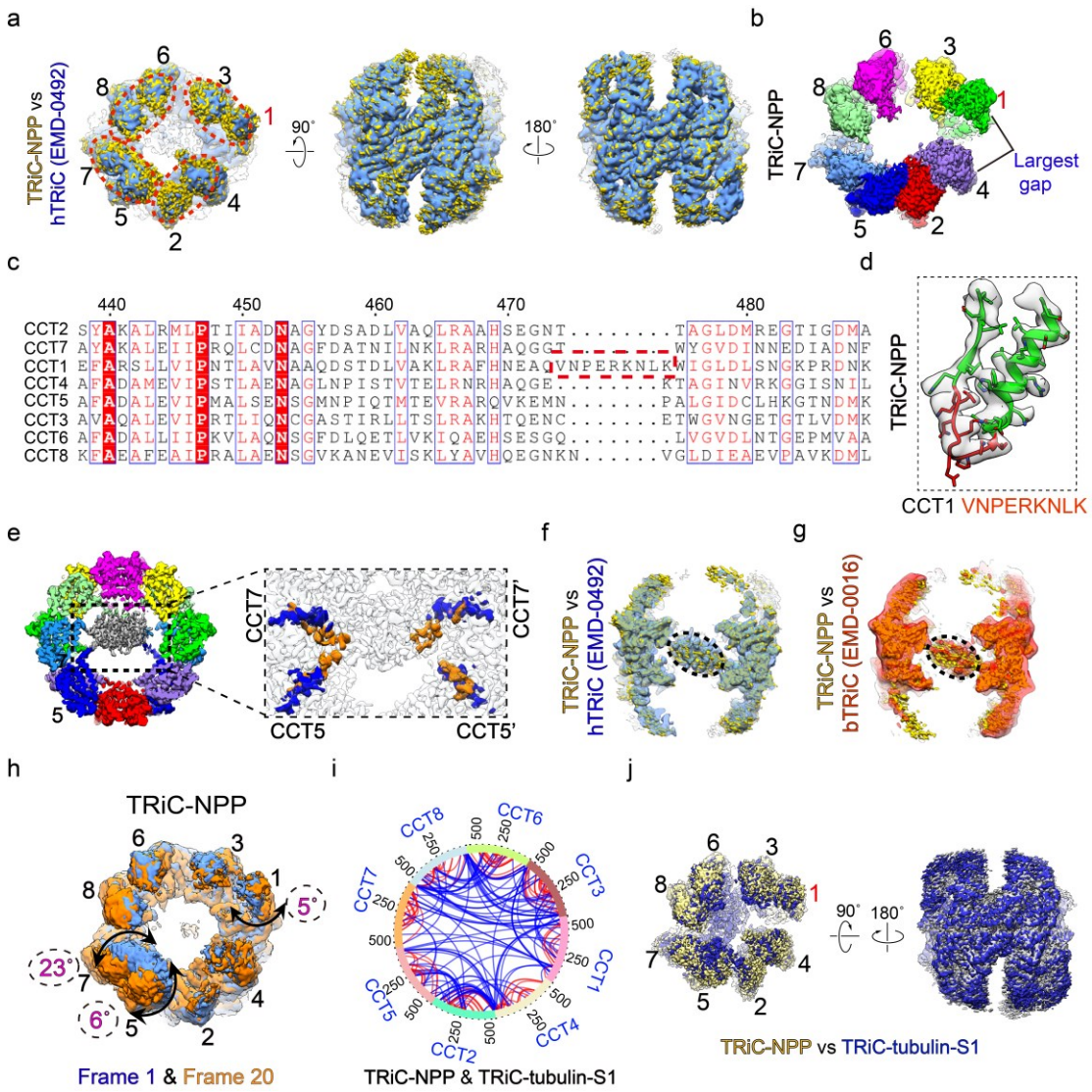

Extended Data Fig. 4 | TRiC-NPP and TRiC-tubulin-S1 conformations and subunit configurations. **a**, Overlay of our TRiC-NPP map (yellow) and the reported apo hTRiC map (cornflower blue, EMDB: 0492), indicating no obvious conformational differences between the two structures. The tetramer-of-dimers pattern is indicated by dotted red circles. **b**, CCT1 and CCT4 display the largest gap between their A domains. **c-d**, Sequence alignment of all the eight subunits of hTRiC, revealing a unique insertion (indicated by red dashed frames) in the E domain of CCT1 (**c**), and the corresponding structural feature of the CCT1 E-domain insertion in TRiC-NPP (**d**). **e**, Depiction of the TRiC-NPP map showing the central tail density symmetrically contacting the N-/C-termini of CCT5/7 and CCT5'/7' from both rings. In the magnified cut-off top view (right), only the resolved N-/C-termini of CCT5/5' and CCT7/7' are colored, with the

1014 C-tails in blue and N-tails in orange. **f-g**, Central slice view of the TRiC-NPP (yellow)
1015 overlaid with apo hTRiC (cornflower blue, EMDB: 0492[49]) (**f**), and with apo bovine
1016 TRiC (red, EMDB: 0016) (**g**), to show their similar tail density features (indicated by
1017 black dashed ellipsoid). **h**, Results for the 3D variability analysis (3DVA) of the TRiC-
1018 NPP dataset. This analysis suggested that CCT7/5/1 underwent a continuous
1019 outward/inward tilting motions of up to ~23°/6°/5°, respectively. Frame 1 (cornflower
1020 blue) and frame 20 (orange), together showing the maximum extent of the
1021 conformational change, are displayed. **i**, XL-MS-derived circular plot of all XLs of the
1022 TRiC portion, with intra-subunit XLs shown in red, and inter-subunit XLs in blue. The
1023 detected cross-links within the TRiC complex fulfill the spatial geometry constrains of
1024 the linked amino acids, validating the reliability of our XL-MS data. **j**, TRiC-NPP map
1025 (yellow) overlaid with the TRiC-tubulin-S1 map (medium blue), indicating no obvious
1026 conformational differences between them.

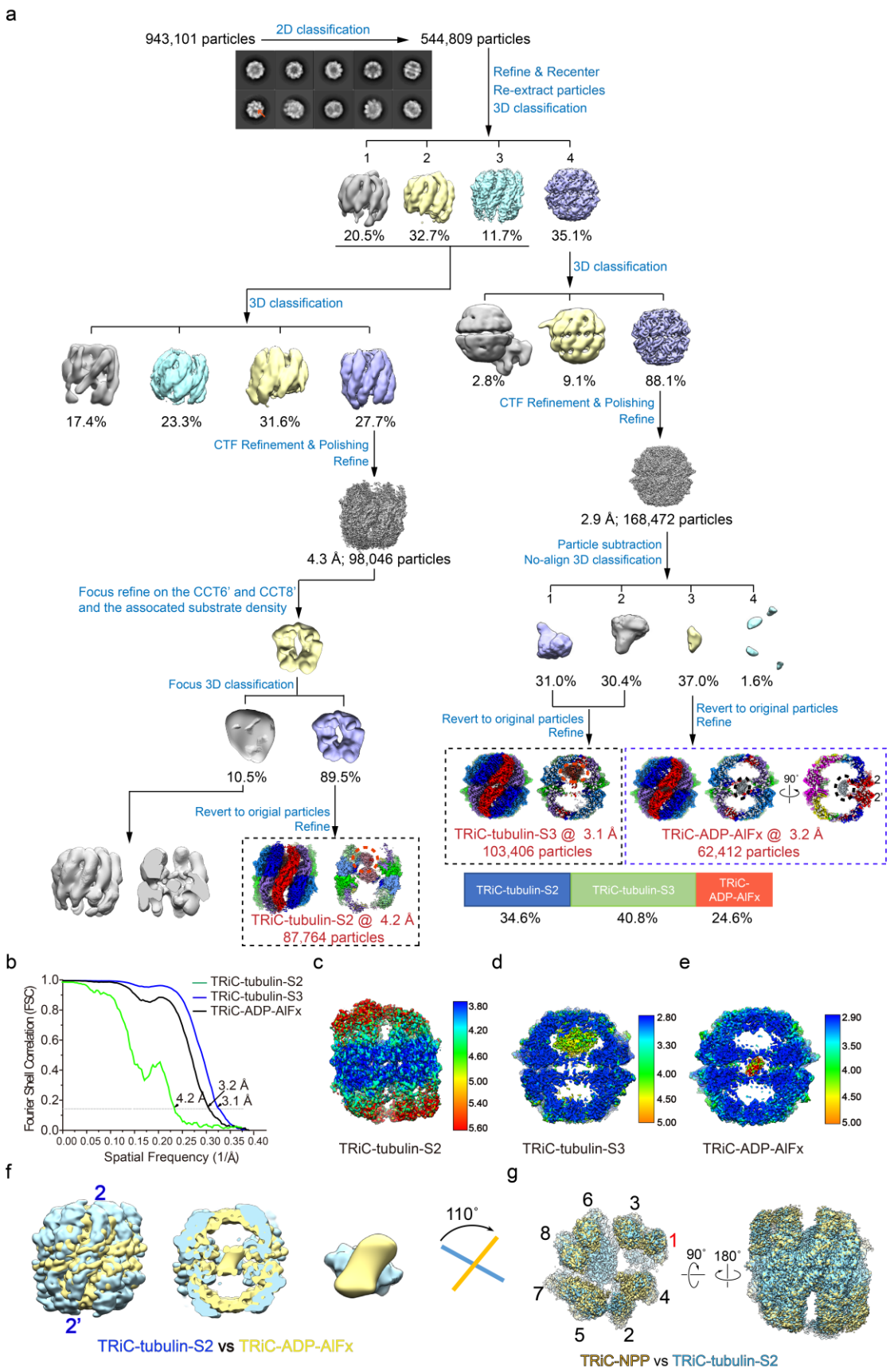

1027

1028 **Extended Data Fig. 5 | Work flow for the processing of the cryo-EM data of TRiC**

in the presence of ATP-AlFx. a, Procedure used to process the cryo-EM data of TRiC in the presence of ATP-AlFx. The reference-free 2D class averages and the population distributions of the three obtained states are also presented. Besides, central slice view of the TRiC-ADP-AlFx map revealed the tail density attached to the CCT2/2' subunit pair. **b**, Resolution estimations of the TRiC-tubulin-S2, -S3, and TRiC-ADP-AlFx maps according to the gold-standard FSC criterion of 0.143. **c-e**, Local resolution evaluations for the S2 (**c**), S3 (**d**), and TRiC-ADP-AlFx (**e**) maps. **f**, Overlay of the TRiC-tubulin-S2 and TRiC-ADP-AlFx maps. When visualized from the typical viewing direction with the CCT2 subunit pair facing the viewer, the unstructured tail of TRiC-ADP-AlFx was observed to be rotated clockwise by about 110° relative to that of TRiC-tubulin-S2. These two maps were lowpass filtered to 8 Å for better visualization of the tail density. **g**, Overlay of the TRiC-NPP (yellow) and -S2 maps (sky blue), indicating their overall similar conformations.

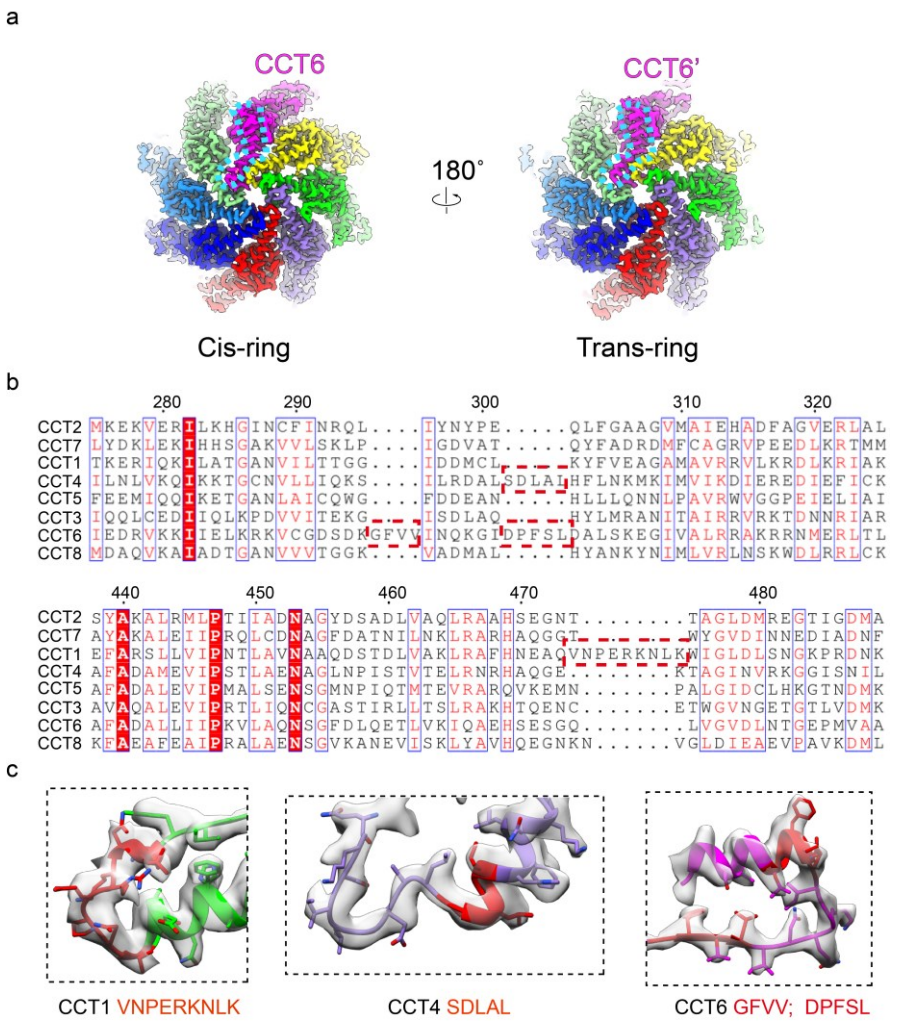

Extended Data Fig. 6 | Features facilitating the subunit identification for the TRiC-tubulin-S3 map. a, Depictions of the S3 map in which the unique kink feature (enclosed in a dotted blue line) in the apical protrusion H8 of CCT6 was unambiguously visualized in both rings, substantiating the on-axis location of CCT6. **b**, Sequence alignment of all eight subunits of hTRiC. This alignment revealed four unique insertions (indicated by red dashed frames) in CCT1/4/6. **c**, Related structures of the four insertions (in red), all resolved in our S3 map.

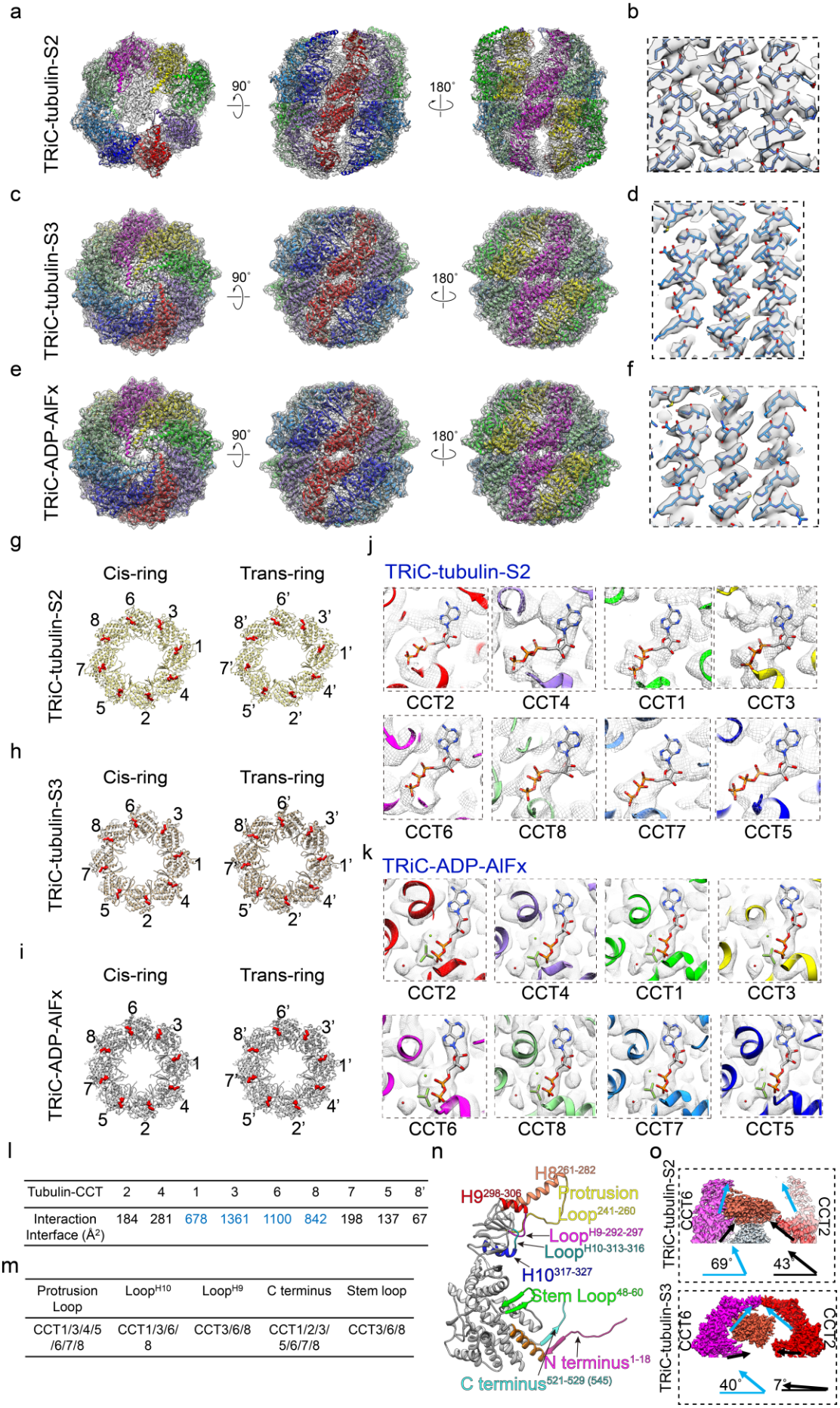

Tubulin-CCT	2	4	1	3	6	8	7	5	8'
Interaction Interface (Å^2)	184	281	678	1361	1100	842	198	137	67

Protrusion Loop	Loop^{H10}	Loop^{H9}	C terminus	Stem loop
CCT1/3/4/5/6/7/8	CCT1/3/6/8	CCT3/6/8	CCT1/2/3/5/6/7/8	CCT3/6/8

1050

1051 **Extended Data Fig. 7 | Atomic models of TRiC-tubulin-S2, -S3, TRiC-ADP-AlFx**
1052 **and nucleotide status in the TRiC-tubulin-S2 and TRiC-ADP-AlFx maps**. **a,c,e**
1053 Atomic models of TRiC-tubulin-S2 (**a**), -S3 (**c**) and TRiC-ADP-AlFx (**e**) match well
1054 with the corresponding cryo-EM maps. **b,d,f**, Representative high-resolution structural
1055 features of TRiC-tubulin-S2 (**b**), -S3 (**d**) and TRiC-ADP-AlFx (**f**). **g-i**, Nucleotide
1056 occupancy statuses of TRiC-tubulin-S2 (**g**), -S3 (**h**) and TRiC-ADP-AlFx (**i**). **j**,
1057 Magnified view of the TRiC-tubulin-S2 nucleotide pocket region of each subunit.
1058 Every subunit appears to include a bound nucleotide density that matches the ATP
1059 model reasonably well, suggesting that the TRiC-tubulin-S2 is in the ATP-bound state.
1060 **k**, Magnified view of the TRiC-ADP-AlFx nucleotide pocket region of each subunit.
1061 Every subunit here was found to be bound with ADP-AlFx (stick model) and a
1062 magnesium ion (green ball), as well as a water molecule (red ball) in an attacking
1063 position, suggesting that each of these subunits is in the ATP-hydrolysis transition state.
1064 **l**, Interaction areas between tubulin and TRiC subunits in TRiC-tubulin-S3 as calculated
1065 using PISA. **m**, Main structural elements of TRiC involved in the interaction with
1066 tubulin in TRiC-tubulin-S3. **n**, Key structural elements of TRiC involved in the
1067 interaction with tubulin, with the residue numbers of these elements being labeled
1068 (CCT3 as a representative subunit). **o**, Depictions of a portion of the S2 and S3 maps
1069 (showing CCT6/2 subunits only), suggesting ATP-hydrolysis-induced TRiC A and E
1070 domain downward rotations. In each panel, showing is the angle between the long axis
1071 of the A (in light blue) or E domain (in black) of CCT2 and the horizontal plane for the
1072 corresponding map.

1073

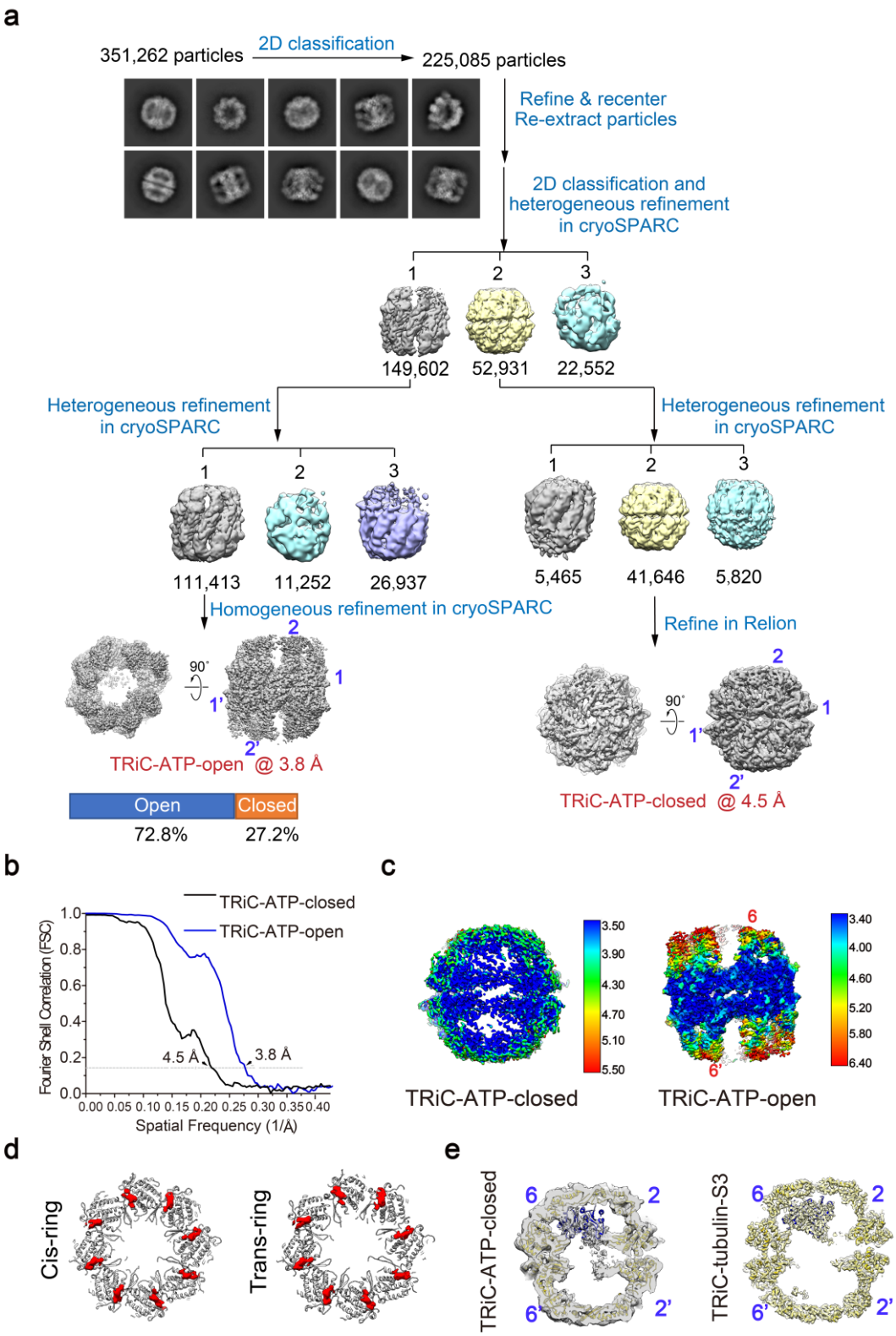

Extended Data Fig. 8 | Cryo-EM analysis of TRiC in the presence of ATP. a, Procedure used to process the cryo-EM data of TRiC in the presence of ATP. Reference-free 2D class averages and population distributions of the closed and open conformations of TRiC (denoted as "TRiC-ATP-closed" and "TRiC-ATP-open",

1079 respectively) are also presented. **b**, Resolution estimations for TRiC-ATP-closed and
1080 TRiC-ATP-open maps according to the gold-standard FSC criterion of 0.143. **c**, Local
1081 resolution evaluations for TRiC-ATP-closed and TRiC-ATP-open. **d**, The nucleotide
1082 occupancy status of TRiC-ATP-closed showed that all nucleotide pockets were
1083 occupied. **e**, The central slice of the TRiC-ATP-closed (left, unsharpened map) and
1084 TRiC-tubulin-S3 (right) map with fitted model of TRiC-tubulin-S3. This analysis
1085 indicates a substrate within one of the TRiC-ATP-closed chambers, in a position and
1086 orientation similar to those of tubulin observed in the TRiC-tubulin-S3 map.

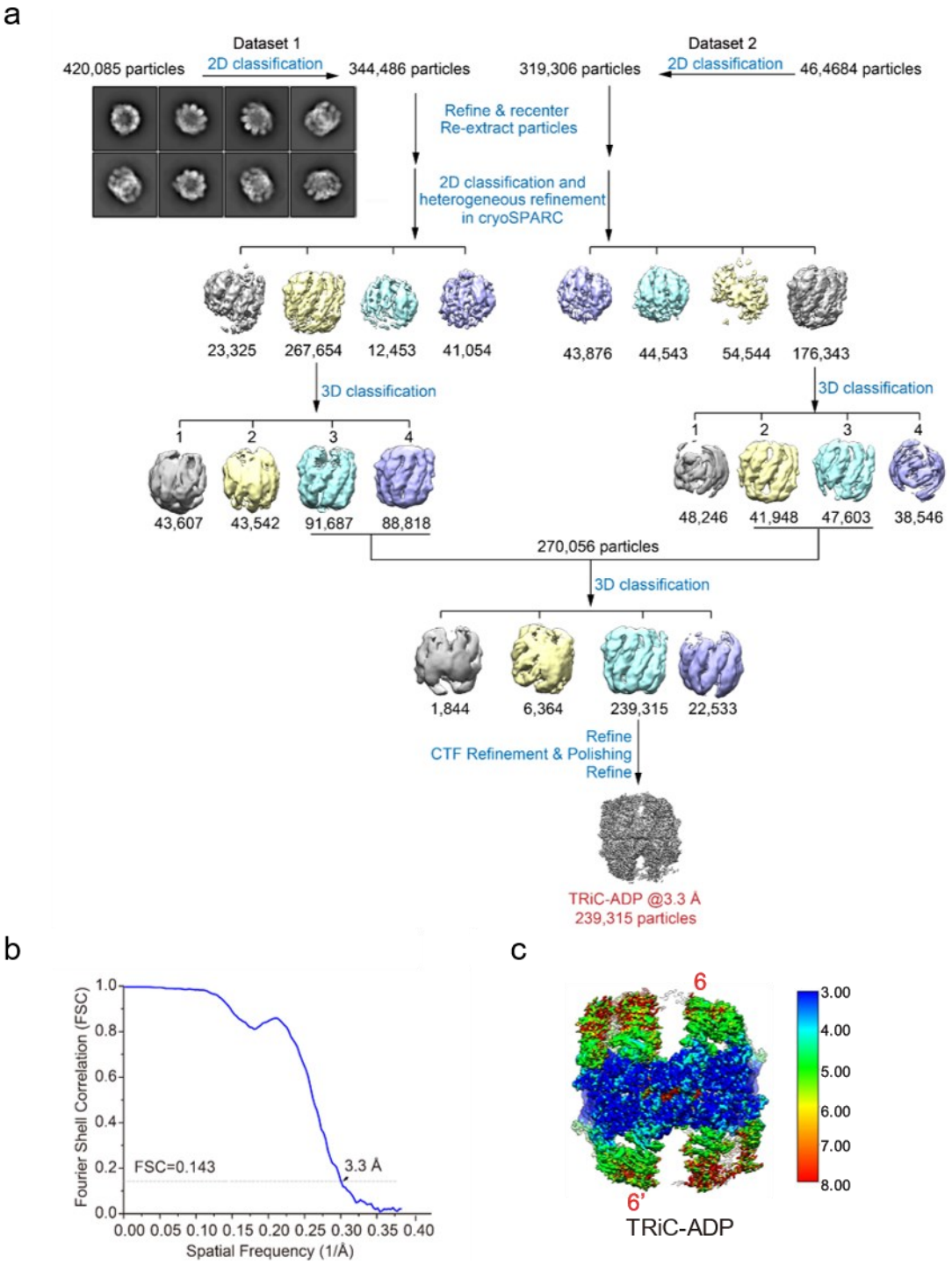

Extended Data Fig. 9 | Work flow for the processing of the TRiC-ADP cryo-EM data. a, Procedure used to process the cryo-EM data of TRiC in the presence of ADP, with the reference-free 2D class average also shown. **b**, Estimation of the TRiC-ADP map resolution according to the gold-standard FSC criterion of 0.143. **c**, Local resolution evaluation for TRiC-ADP.

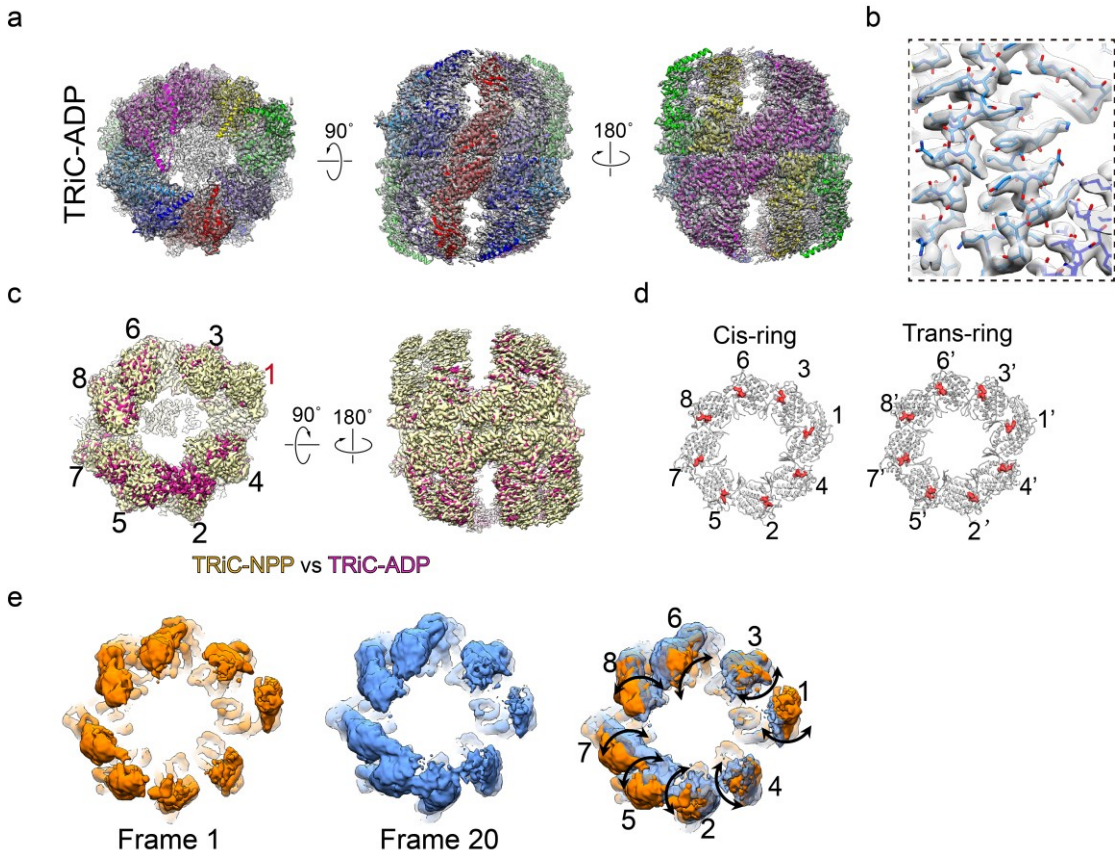

Extended Data Fig. 10 | Atomic model and 3DVA result of TRiC-ADP. a, Atomic model of TRiC-ADP matches well with the corresponding map. **b**, Representative high-resolution structural features of TRiC-ADP. **c**, The determined nucleotide occupancy status of TRiC-ADP, showing all of the subunit nucleotide pockets were occupied. **d**, Overlay of the TRiC-NPP (yellow) and TRiC-ADP (violet red) maps, indicating no large conformational differences between them. **e**, 3DVA results of the TRiC-ADP dataset. This analysis suggested that all of the subunits underwent outward/inward tilting motions. Frames 1 (orange) and 20 (cornflower blue), together showing the maximum extent of the conformational change, are displayed here.

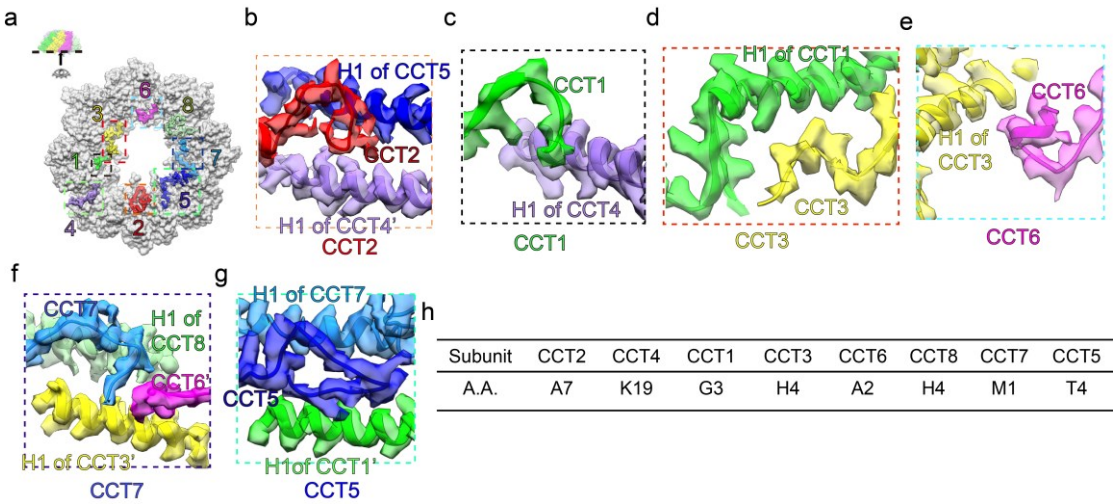

Subunit	CCT2	CCT4	CCT1	CCT3	CCT6	CCT8	CCT7	CCT5
A.A.	A7	K19	G3	H4	A2	H4	M1	T4

Extended Data Fig. 11 | The involvement of the TRiC N-termini in the allosteric interaction network in TRiC-tubulin-S3. a, Locations of the resolved N-termini (in color) in the TRiC-tubulin-S3 structure. The visualization direction and visualized region are illustrated in the inset. **b-g**, Magnified views of the interaction between the N-terminus of CCT2 and helices H1 of CCT5 and CCT4' (**b**), between the N-terminus of CCT1 and H1 of CCT4 (**c**), between the N-terminus of CCT3 and H1 of CCT1 (**d**), between the CCT6 N-terminus (there is a small 1-turn α-helix before its N-terminal β-sheet) and H1 of CCT3 (**e**), between the N-terminus of CCT7 and H1 of CCT8 and CCT3', as well as the N-terminus of CCT6' (**f**), and between the N-terminus of CCT5 and helices H1 of CCT7 and CCT1'(**g**). **h**, The most N-terminal amino acid residue visualized for each subunit of TRiC in the TRiC-tubulin-S3 structure.

1116 **Table 1 | Cryo-EM data collection, processing, and model validation statistics**

	TRiC-NPP (EMDB-32922) (PDB-7X0A)	TRiC-tubulin-S1 (EMDB-32903) (PDB-7WZ3)	TRiC-tubulin-S2 (EMDB-32989) (PDB-7X3J)	TRiC-tubulin-S3 (EMDB-32923) (PDB-7X0S)	TRiC-ADP-AlFx (EMDB-32926) (PDB-7X0V)	TRiC-ADP (EMDB-32993) (PDB-7X3U)	TRiC-ATP-closed (EMDB-33025) (PDB-7X6Q)	TRiC-ATP-open (EMDB-33053) (PDB-7X7Y)
Data collection and processing								
Magnification				18,000			81,000	
Voltage (kV)				300			300	
Detector				K2 summit			K3	
Electron exposure (e–/Å²)				38			50	
Defocus range (μm)				-0.8 to -2.5			-0.8 to -2.5	
Pixel size (Å)				1.318			0.89	
Symmetry imposed				C1			C1	
Initial particle images (no.)	761,665	761,665	943,101	943,101	943,101	884,769	351,262	351,262
Final particle images (no.)	185,216	115,666	87,764	103,406	62,412	239,315	41,646	111,413
Map resolution (Å)	3.1	4.1	4.2	3.1	3.2	3.3	4.5	3.8
FSC threshold				0.143				
Map resolution range (Å)	3.0-8.0	3.8-8.4	3.8-8.4	2.8-4.5	2.9-4.5	3.0-8.0	3.5-5.5	3.4-6.4
Refinement								
Initial model used (PDB code)	5GW4; 5GW5	5GW4; 5GW5	5GW4; 5GW5	6KS6; 5JCO	6KS6	5GW4; 5GW5	6KS6	5GW4; 5GW5
Model resolution (Å)	4.2	7.4	7.2	3.4	3.6	3.6	4.5	4.2
FSC threshold				0.5				
Map sharpening *B* factor (Å²)	-76.7	-133.7	-144.4	-53.3	-80.4	-96.2	-135.8	-111.4
Model composition								
Non-hydrogen atoms	63,694	58,818	63,464	63,367	65,020	63,964	64,486	63,532
Protein residues	8,314	7,686	8,241	8,866	8,440	8,314	8,440	8,314
Ligands	6	6	16	48	48	16		
B factors (Å²)								
Protein	120.55	127.93	31.20	55.75	79.70	33.58	55.28	179.95
Ligand	57.86	45.81	11.53	51.16	72.45	8.06		
R.m.s. deviations								
Bond lengths (Å)	0.005	0.004	0.005	0.003	0.004	0.003	0.091	0.003
Bond angles (°)	0.533	0.996	1.105	0.665	1.072	0.655	1.669	0.886
Validation								
MolProbity score	1.39	1.13	1.40	1.43	1.54	1.17	1.35	1.44
Clashscore	3.67	2.17	4.21	3.19	4.23	1.78	3.45	5.18
Poor rotamers (%)	0.04	0.00	0.07	0.04	0.04	0.07	0.01	0.00
Ramachandran plot								
Favored (%)	96.50	97.25	96.82	95.36	95.10	96.48	96.68	97.09
Allowed (%)	3.47	2.75	3.17	4.64	4.90	3.43	3.16	2.91
Disallowed (%)	0.03	0.00	0.01	0.00	0.00	0.09	0.15	0.00

1117

1118 **Supplementary Table 1 | Results of mass spectroscopy (MS) analysis of**
1119 **endogenously purified TRiC with associated tubulin**

	Protein	Coverage	PSMs	Peptides	Unique peptides
TRiC subunits	CCT1	79	116	39	37
	CCT2	78	199	36	36
	CCT3	73	113	41	41
	CCT4	72	125	33	32
	CCT5	68	139	41	39
	CCT6	64	124	35	30
	CCT7	80	194	39	32
	CCT8	75	121	40	40
TUBB	TUBB5	82	104	47	9
	TUBB4	38	31	16	3
	TUBB2	44	27	14	3
	TUBB6	24	12	7	2
	TUBA4	7	3	3	1
	TUBG1	24	7	6	6
	TUBD1	6	2	2	2

1120

1121 **Supplementary Table 2 | Results of XL-MS analysis of TRiC with associated**

1122 **tubulin**

Protein1 (site) –Protein2 (site) Inter-Protein	Peptides	Score	Spec count
CCT3 (21)-Tubulin (58)	KVQSGNINAAK(1)-ISVYYNEATGGKYVPR(12)	9.35E-09	3
CCT3 (21)-Tubulin (252)	KVQSGNINAAK(1)-KLAVNMVPFPR(1)	7.00E-10	4
CCT4 (21)-Tubulin (58)	GKGAYQDR(2)-ISVYYNEATGGKYVPR(12)	1.42E-22	3
CCT6 (10)-Tubulin (252)	TLNPKAEVAR(5)-KLAVNMVPFPR(1)	8.44E-07	4
CCT8 (16)-Tubulin (252)	APGFAQMLKEGAK(9)-KLAVNMVPFPR(1)	5.15E-06	2

1123

1124 * We used E-value (1.00E-02) and spec count (larger than 1) as the threshold to remove

1125 extra XL-MS data with low confidence.

1126 **Supplementary Table 3 | Results of XL-MS analysis of TRiC with associated**
1127 **tubulin in the presence of ATP-AlFx**

Protein1 (site) –Protein2 (site) Inter-Protein	Peptides	E-value	Spec count
CCT1 (532)-Tubulin (252)	IDDLIKLHPESK(6)-KLAVNMVPFPR(1)	3.12E-04	3
CCT2 (250)-Tubulin (252)	IKIFGSR(2)-KLAVNMVPFPR(1)	5.03E-06	3
CCT2 (522)-Tubulin (252)	VDNIIKAAPR(6)-KLAVNMVPFPR(1)	2.24E-14	9
CCT2 (248)-Tubulin (252)	ILIANTGMDTDKIK(12)-KLAVNMVPFPR(1)	8.77E-05	3
CCT3 (21)-Tubulin (58)	KVQSGNINAAK(1)-ISVYYNEATGGKYVPR(12)	6.03E-08	3
CCT3 (527)-Tubulin (252)	IDDIVSGHKK(9)-KLAVNMVPFPR(1)	1.20E-10	5
CCT3 (21)-Tubulin (252)	KVQSGNINAAK(1)-KLAVNMVPFPR(1)	1.61E-10	4
CCT3 (248)-Tubulin (252)	IVLLDSSLEYKK(11)-KLAVNMVPFPR(1)	5.19E-05	3
CCT4 (2)-Tubulin (252)	PENVAPR(1)-KLAVNMVPFPR(1)	9.06E-11	8
CCT5 (263)-Tubulin (252)	HKLDVTSVEDYK(2)-KLAVNMVPFPR(1)	1.12E-12	4
CCT5 (257)-Tubulin (252)	IAILTCPFEPPKPK(12)-KLAVNMVPFPR(1)	1.55E-05	3
CCT6 (10)-Tubulin (252)	TLNPKAEVAR(5)-KLAVNMVPFPR(1)	2.37E-20	4
CCT7 (55)-Tubulin (252)	GKATISNDGATILK(2)-KLAVNMVPFPR(1)	1.01E-21	4
CCT8 (296)-Tubulin (252)	AIADTGANVVVTGGKVADMALHYANK(15)-KLAVNMVPFPR(1)	2.39E-10	8
CCT8 (225)-Tubulin (58)	KETEGDVTSVK(1)-ISVYYNEATGGKYVPR(12)	4.44E-08	3
CCT8 (225)-Tubulin (252)	KETEGDVTSVK(1)-KLAVNMVPFPR(1)	1.36E-08	2
CCT8 (318)-Tubulin (252)	LNSKWDLR(4)-KLAVNMVPFPR(1)	5.09E-13	5

1128

1129 * We used E-value (1.00E-02) and spec count (larger than 1) as the threshold to remove
1130 extra XL-MS data with low confidence.

Supplementary Table 4 | Interactions between tubulin and CCT3/6/8/1 detected using PISA

	TRiC subunit		Tubulin		Interaction	Distance (Å)
	Residue	Atom	Residue	Atom		
CCT3	GLU 89	[OE1]	LYS 392	[NZ]	Salt bridge/ H bond	3.82
	GLU 69	[OE2]	HIS 396	[NE2]	Salt bridge	3.32
	ARG 313	[NE]	GLU 157	[OE2]	Salt bridge	3.72
	ARG 200	[NH1]	ASP 404	[OD2]	Salt bridge/ H bond	3.65
	ARG 316	[NH1]	GLU 407	[OE2]	Salt bridge/ H bond	3.71
	LYS 317	[NZ]	GLU 410	[OE1]	Salt bridge/ H bond	2.52
	LYS 317	[NZ]	GLU 410	[OE2]	Salt bridge	3.87
	LYS 196	[NZ]	GLU 405	[OE2]	Salt bridge	3.90
	GLU 69	[OE1]	TRP 397	[NE1]	H bond	3.74
	GLU 69	[OE2]	TRP 397	[NE1]	H bond	3.64
	ARG 316	[NH1]	TYR 106	[OH]	H bond	2.48
	ARG 85	[NH1]	ARG 391	[O]	H bond	2.83
	ARG 68	[NH2]	LYS 392	[O]	H bond	3.74
	LYS 203	[NZ]	GLY 400	[O]	H bond	3.30
	ARG 200	[NH1]	MET 403	[O]	H bond	3.33
	ARG 200	[NH2]	MET 403	[O]	H bond	3.49
	ASN 321	[ND2]	MET 406	[SD]	H bond	3.26
	THR 318	[OG1]	GLU 407	[OE2]	H bond	3.03
CCT6	ASP 213	[OD1]	ARG 121	[NH1]	Salt bridge/ H bond	3.22
	ASP 213	[OD1]	ARG 121	[NH2]	Salt bridge	3.41
	ASP 213	[OD2]	LYS 122	[NZ]	Salt bridge/ H bond	2.45
	ARG 319	[NH1]	ASP 114	[OD2]	Salt bridge	3.49
	ARG 319	[NH2]	ASP 114	[OD2]	Salt bridge/ H bond	2.73
	ARG 314	[NH2]	ASP 128	[OD1]	Salt bridge/ H bond	3.17
	ARG 318	[NH1]	GLU 157	[OE1]	Salt bridge/ H bond	3.27
	GLU 357	[OE1]	THR 55	[OG1]	H bond	2.84
	ARG 315	[O]	ARG 121	[NH1]	H bond	3.28
	ASP 213	[OD2]	ARG 121	[NH2]	H bond	2.44
	TYR 239	[O]	ARG 162	[NH1]	H bond	3.48
	ALA 51	[N]	ASP 74	[OD2]	H bond	3.58
	ARG 314	[NH2]	GLU 125	[O]	H bond	2.48
	ARG 314	[NH1]	ASP 128	[O]	H bond	3.89
	ARG 217	[NE]	GLU 125	[O]	H bond	3.04
	GLY 215	[N]	GLU 125	[OE2]	H bond	3.79
	GLU 238	[OE1]	LEU 130	[N]	H bond	3.75
	GLN 294	[NE2]	GLU 158	[OE1]	H bond	2.69
CCT8	GLU 252	[OE1]	ARG 2	[NE]	Salt bridge/ H bond	3.27
	GLU 252	[OE1]	ARG 2	[NH2]	Salt bridge/ H bond	3.26
	ARG 314	[NE]	ASP 41	[OD2]	Salt bridge	3.69
	ARG 314	[NH1]	ASP 41	[OD1]	Salt bridge	3.51
	LYS 318	[NZ]	ASP 128	[OD2]	Salt bridge/ H bond	3.58
	GLU 252	[O]	ARG 2	[NH2]	H bond	2.98
	LYS 225	[NZ]	TYR 36	[OH]	H bond	3.67
	ARG 314	[NH1]	ASP 41	[OD2]	H bond	2.97
	ASN 316	[ND2]	ASP 41	[OD1]	H bond	2.68
	SER 317	[OG]	GLU 53	[OE2]	H bond	2.34
	LYS 318	[N]	GLU 53	[OE1]	H bond	3.28
	TRP 319	[NE1]	GLU 53	[O]	H bond	2.66
CCT1	ARG 309	[NH2]	GLU 410	[OE1]	Salt bridge/ H bond	3.66
	ASP 358	[O]	LYS 392	[NZ]	H bond	2.94
	GLN 242	[NE2]	ASP 417	[OD1]	H bond	3.81
	GLN 242	[OE1]	GLN 424	[NE2]	H bond	3.55
	ARG 310	[NH2]	ASN 416	[O]	H bond	3.31
	ARG 310	[NH2]	SER 420	[OG]	H bond	2.74

Supplementary Video Legends

Supplementary Video 1 | 3D variability analysis (3DVA) of the TRiC-NPP cryo-EM data. The 3DVA results suggested that the A/I domains of CCT1/4/2/5/7 subunits are overall relative dynamic, with those of CCT7/5/1 even displaying larger movements.

Supplementary Video 2 | 3D variability analysis (3DVA) of the TRiC-ADP cryo-EM data. The 3DVA results suggested that TRiC-ADP was very dynamic with all of the subunits, including the usually most stable CCT6 subunit, displaying an outward/inward tilting motion.